American Mineralogist, Volume 89, pages 665–680, 2004

Raman spectroscopy of Fe-Ti-Cr-oxides, case study: Martian meteorite EETA79001

ALIAN WANG,* KARLA E. KUEBLER, BRADLEY L. JOLLIFF, AND LARRY A. HASKIN

Department of Earth and Planetary Sciences and McDonnell Center for Space Sciences, Washington University, St. Louis, Missouri 63130, U.S.A.

ABSTRACT

Raman spectral features of chromite, ulvöspinel, magnetite, ilmenite, hematite, and some of their solid solutions are presented. Although most Fe-Ti-Cr-oxides produce relatively weak Raman signals compared to oxyanionic minerals, sufficient information can be extracted from their spectra to identify the end-member mineral phases as well as some information about compositional variations in solid solutions. Correlations between Raman spectral features and mineral chemistry are used to interpret the Raman data of Fe-Ti-Cr oxides found during Raman point-count measurements on rock chips of Martian meteorite EETA79001, as an analog to Mars on-surface planetary investigations. In general, ulvöspinel, magnetite, and chromite end-members are readily distinguished by their Raman spectral patterns, as are ilmenite and hematite. In the low signal-to-noise (S/N) spectra generally obtained from the Raman point-count procedure, the position and shape of the strongest peak of Fe-Ti-Cr oxides in the region 660–680 cm^{-1} (A_{1g} mode) is the most useful for discriminating Fe^{3+}-Ti-Cr-Al substitutions in the magnetite-ulvöspinel, ulvöspinel-chromite, and chromite-spinel series, but minor peaks in the range 300–600 cm^{-1} also assist in discrimination. These spectral features are useful for investigating the variability among Fe-Ti-Cr-Al oxide solid solutions in natural samples. In EETA79001, a Martian basaltic meteorite, most of the oxide grains (as measured with the electron microprobe) are ulvöspinel, chromian ulvöspinel, and chromite, but ilmenite, titanian chromite, and titanomagnetite are also observed. The Fe-Ti-Cr-oxides identified by Raman point-count include end-member ilmenite, low-Al chromite-spinel solid solutions, ulvöspinel-magnetite solid solutions, and more complex chromite-spinel-ulvöspinel-magnetite solid solutions; the latter exhibit a wide range of main peak positions and broadened peak widths that may reflect structural disorder as well as specific cation contents. One Raman spectrum suggests end-member magnetite, and one spectrum from a different rock chip appears to be that of non-terrestrial hematite, reflecting local oxidizing alteration, which has not been observed previously in this meteorite. These results show that analyses done in an automated mode on the surface of an unprepared Martian rock sample can provide useful constraints on the Fe-Ti-Cr oxide mineralogy present and on compositional variations within those minerals, including an indication of oxygen fugacity.

INTRODUCTION

Laser Raman spectroscopy is anticipated to be a powerful technique for characterization of materials on the surfaces of planets, satellites, and asteroids (Wang et al. 1995). Raman spectroscopy can provide straightforward, unambiguous identification of major rock-forming minerals (e.g., silicates and carbonates; Wang et al. 1994, 1999a), accessory minerals (e.g., phosphates, oxides, and sulfides; Kuebler et al. 2002), and secondary minerals produced by weathering, aqueous precipitation, and hydrothermal alteration (e.g., sulfates, carbonates, zeolites, Fe oxides, and phyllosilicate clay minerals; Wang et al. 1999b, 2002; Wang and Valentine 2002; Kuebler et al. 2001). Raman spectroscopy can also provide information on structural and compositional variants of many mineralogical groups. Rock types can be inferred from sequences of Raman spectra (Haskin et al. 1997). Raman spectroscopy can also identify OH, bound and unbound forms of water, and organic and graphitic carbon at low concentrations (Wdowiak et al. 1997; Wang et al. 2001a), including organic compounds pertinent to the detection of life (e.g., Edwards et al. 1999; Wynn-Williams and Edwards 2000; Wang et al. 2001b). It is feasible to build a small Raman system as part of an instrument payload for a rover or a lander to carry out on-surface analyses (Wang et al. 1998; Haskin et al. 2001, 2002; Wang et al. 2003).

Here, we demonstrate the characterization of Fe-Ti-Cr oxides using Raman spectroscopy. The identifications and compositions of these minerals provide information and constraints on conditions of rock genesis and alteration. Most previous Raman spectroscopic studies of opaque minerals, especially the Fe-Ti-Cr-oxides, have been concerned with synthetic or end-member specimens, and they have emphasized spectral peak assignments and the structural significance of spectral features. In nature, most opaque phases occur as solid solutions. Some solid-solution series exhibit changes in crystal structure that can be related to their chemical compositions. For on-surface Raman spectroscopy, we need to determine the basic Raman spectral features of these minerals and the effects of compositional and structural variations on spectral patterns and peak positions, and to do so under conditions that mimic on-surface planetary work. Thus,

* E-mail: alianw@levee.wustl.edu

in this study, we use data on well-characterized Fe-Ti-Cr oxide samples to study the spectral patterns and peak positions of oxide minerals of different chemical compositions. Then, we apply this information to spectral data from Martian meteorite EETA79001 as an analog to Mars on-surface planetary investigations.

In a Raman spectroscopic experiment, the composition of a mineral grain is not measured directly but is extracted from Raman peak position shifts. More accurate determinations of chemical composition can be achieved in the laboratory using instruments such as the electron microprobe; however, during recent and near-term planetary surface exploration missions, the primary method to determine chemical composition (Alpha Proton X-ray Spectrometer) provides data for whole rocks or soil. No methods currently are in use or planned to determine chemical composition of individual mineral phases. The Mars microbeam Raman spectrometer (MMRS) under development is designed to take hundreds of spectra along a linear traverse on the surface of a rock or soil sample, and each spectrum will reflect contributions from only one or a few mineral phases (grains). Extracting compositional information from each spectrum, in addition to mineral identification, will be useful for interpreting the mineral-forming processes.

Samples and experiments

We used a HoloLab5000 Raman system (Kaiser Optical System Inc.) equipped with an automated scanning stage for the Raman spectroscopic measurements of this study. Samples were analyzed with two laser frequencies, the 632.8 nm line of a He-Ne laser and the 532 nm line of a frequency-doubled Nd:YAG laser. The laser beam was unpolarized at the sample. The spectrometer has a spectral resolution of 4–5 cm^{-1}. A 20×, long-working-distance objective (0.4 NA) was used for all of the measurements. The wavelength calibration of the HoloLab-5000 system was established by least-squares curve fitting of a set of measured Ne lines to standard values. The wavenumber accuracy is better than 0.5 cm^{-1} in the spectral region of interest. The wavenumber reproducibility was checked using the Raman peak of a Si wafer each working day, and was better than ~0.3 cm^{-1} over several months.

We used a JEOL 733 electron microprobe with a back-scattered electron (BSE) detector, three wavelength-dispersive spectrometers, and Advanced Microbeam automation for the electron-microprobe analyses. The accelerating voltage was 15 kV, the beam current was 30–40 nA, and the beam diameter was 1–20 μm. We used a combination of magnetite, V_2O_5, rutile, gahnite, rhodonite, Cr_2O_3, and spinel standards. X-ray matrix corrections were based on a modified Armstrong (1988) CITZAF routine incorporated into the electron-microprobe software. From the oxides analyses, molar cation values of Fe^{2+}, Fe^{3+}, Mg^{2+}, Cr^{3+}, Ti^{4+}, Mn^{2+}, V^{3+}, Al^{3+}, Ca^{2+}, Zn^{2+}, and Si^{4+} were calculated using the measured weight percentages of corresponding oxides based on either three or four oxygen atoms (corundum or spinel structure) per formula unit, as appropriate.

Table 1 lists representative chemical compositions obtained by EMP analyses of the standard Fe-Ti-Cr-oxide samples studied in this work. Raman spectra and compositional data were obtained from the same grain from each sample. Single mineral grains (hundreds of micrometers to millimeters in size) were mounted on the tops of brass bars, which were inserted into standard holders for EMP analyses. Several Raman spectra were taken on each grain before mounting and after the EMP analyses.

Five rock chips and three thin sections of Martian meteorite EETA79001 were studied. EETA79001 is a pyroxene-rich basaltic shergottite. It consists mostly of two igneous lithologies (A and B) separated by an igneous or impact-melt contact. The two lithologies are related, but differ in texture and in mineral assemblages and compositions. Pigeonite, augite, and plagioclase (maskelynite) are the major phases in both, but lithology A contains coarse xenocrysts or xenoliths of olivine and orthopyroxene that are more magnesian than those of the finer grained basaltic matrix. The groundmass of lithology A has an average grain size of ~0.15 mm and no preferred orientation. The groundmass of lithology B is mineralogically similar to that of A, but is coarser (mean grain size ~0.35 mm) and represents a more differentiated composition [e.g., pyroxene compositions are more extensively zoned to high-Fe concentrations (McSween and Jarosewich 1983; Mittlefehldt et al. 1997)].

In Martian meteorite EETA79001, ulvöspinel, Al-chromite, Al-Ti-chromite, high Cr-ulvöspinel, Cr-ulvöspinel, ilmenite, and rare titanomagnetite have been identified in thin sections and in small rock chips (Table 2). For a subset of the oxide grains, we obtained Raman spectra at the same sample spots where electron microprobe analyses were acquired in two thin sections (TS442 of lithology A and TS357 of lithology B). Co-registration of the sample spots for Raman and EMP analyses was done visually using recognizable microscopic features on the thin sections. This co-registration enables us to determine the effects of compositional variation on Raman spectral features for these solid solutions. BSE images of some Fe-Ti-Cr oxide grains analyzed in thin section by both methods are shown in Figure 1.

Raman spectra were taken with the excitation laser beam in focus at the surface of the sample. A 20× long-working-distance objective provides a condensed laser beam ~6 μm in diameter. Because high excitation laser power may cause local heating in dark-colored minerals, some opaque phases (some Fe-oxides and sulfides) can be altered on warming in the oxidizing laboratory environment. To minimize or prevent this alteration, a reduced laser power ~5 mW was used for most experiments. The most easily oxidized samples (ulvöspinel and magnetite) were shielded from the laboratory atmosphere in an enclosure under flowing dry N_2 gas, and a laser power of only ~2 mw was used. Raman peaks of oxide minerals tend to be substantially broader than those of oxyanionic minerals (e.g., carbonates, sulfates, phosphates, silicates). Because of this difference, there is some peak overlap in Raman spectra of Fe-Ti-Cr oxides, so we used the spectral curve fitting routine of GRAMS/32 to extract information on peak positions and peak widths.

Raman point-counting measurements were made on five rock chips of EETA79001 [one chip from sample EETA79001,476 (lithology A), and four chips from sample EETA79001,482, (lithology B)]. These measurements simulate the type of automated point-count traverses anticipated for Raman measurements on unprepared rock surfaces in the field (Haskin et al. 1997). Automatic focusing is an unnecessary complication for a simple field Raman spectrometer, especially one to be deployed by a robotic arm. In this Raman point-count procedure, a 20× long-working-distance objective and the automatic scanning stage of the HoloLab5000 were used. The stage moves the sample laterally beneath the laser beam along a linear traverse or on a rectangular grid, with spectra taken at selected intervals. For each linear traverse or grid, the laser beam was focused only at the starting point and no focal adjustment was made before taking subsequent spectra. The sample surface was thus a little above or below the laser focal plane at most points because the rock surface was rough. As a consequence, the signal-to-noise (S/N) ratio of many spectra obtained in this way is somewhat lower than would be the case for in-focus Raman measurements, and the sampling volumes in most measurements are larger than those on a polished section. For the lower S/N spectra obtained in point-count measurements, the peak positions were obtained by visually locating the symmetric center of each peak after baseline subtraction of the raw spectra. The precision of determining Raman peak positions by this method is estimated to be ±1 cm^{-1}.

General Raman features of Fe-Ti-Cr-oxides

The Fe-Ti-Cr-oxides that are of greatest interest for igneous mineralogy and petrology are chromite, ulvöspinel, magnetite, ilmenite, hematite, and their solid solutions. They belong to two structural types: the spinel structure and the corundum (or ilmenite) structure. Previous Raman studies on these two structures have concentrated on the high-pressure and high-temperature forms of silicates (or their variants) related to mantle mineralogy, such as Mg_2SiO_4, $MgGe_2O_4$, $MgAl_2O_4$, and Ni_2SiO_4 of the spinel structure, and $MgSiO_3$, $MgGeO_3$, $ZnSiO_3$, $ZnGeO_3$, $MgTiO_3$, and $MnTiO_3$ of the ilmenite structure (Akaogi et al. 1984; Baran and Botto 1979; Baran and Botto 1986; Chopelas and Hofmeister 1991; Chopelas 1999; Cynn et al. 1992; Hofmeister 1993; Hofmeister and Ito 1992; Ishii et al. 1982; Leinenweber et al. 1989; Linton et al. 1999; Liu et al. 1994; McMillan and Akaogi 1987; McMillan and Ross 1987; Reynard and Rubie 1996; Reynard and Guyot 1994; Ross and McMillan 1984; Ross and Navrosky 1987; Ross and Navrotsky 1988;Yamanitsu and Ishii 1986). Very few studies of actual Fe-oxides of these structures have been published (Bersani et al. 1999; De Faria et al. 1997; Kustova et al. 1992; Pinet et al.

TABLE 1. Representative electron microprobe analyses of standard mineral samples

	Mg-Al Chromite	Mg Chromite	Chromian Pleonaste	Magnetite	Ulvöspinel	Ilmenite		Hematite	
Sample	LN_50	84*	HB	synthetic	USP100-1200	20*	497-5*	497-2*	HMS3†
FeO(t)	20.03	21.04	12.80	92.05	64.03	36.47	27.18	78.73	88.74
MgO	12.27	8.14	17.99	0.00	0.00	9.75	0.00	0.00	0.14
Cr_2O_3	55.45	66.51	34.93	0.00	0.00	0.20	0.00	0.00	–
TiO_2	0.80	0.02	0.20	0.06	36.15	50.50	52.54	11.25	0.03
MnO	0.28	0.36	0.10	0.14	0.00	0.25	12.83	0.14	0.00
V_2O_3	0.19	0.05	0.14	0.00	0.00	0.06	0.00	0.00	–
Al_2O_3	8.83	3.54	31.93	0.01	0.00	0.54	0.00	0.00	0.39
CaO	0.01	0.00	0.00	0.01	0.00	0.02	0.00	0.01	0.06
ZnO	0.03	0.08	0.08	0.00	0.00	0.00	7.00	0.09	–
SiO_2	0.09	0.01	0.10	0.00	0.08	0.04	0.00	0.03	1.06
Oxide Sum	98.0	99.7	98.3	92.3	100.3	97.8	99.6	90.3	90.4
FeO	14.61	19.67	9.17	30.64	64.02	27.73	27.18	9.85	0.19
Fe_2O_3	6.02	1.52	4.03	68.24	0.01	9.72	0.00	76.54	97.40
Corr. Sum‡	98.6	99.9	98.7	99.1	100.3	98.8	99.6	97.9	99.3
Number of cations on the basis of 4 oxygen atoms for spinels, 3 for ilmenite and hematite									
Si	0.003	0.000	0.003	0.000	0.003	0.001	0.000	0.001	0.029
Al	0.345	0.144	1.093	0.000	0.000	0.015	0.000	0.000	0.012
Ti	0.020	0.000	0.004	0.002	1.006	0.903	1.006	0.227	0.001
V^{3+}	0.005	0.001	0.003	0.000	0.000	0.001	0.000	0.000	0.000
Cr	1.455	1.815	0.802	0.000	0.000	0.004	0.000	0.000	0.000
Fe^{3+}	0.150	0.039	0.088	1.996	0.000	0.174	0.000	1.545	1.822
Fe^{2+}	0.405	0.568	0.223	0.996	1.982	0.551	0.579	0.221	0.182
Mn^{2+}	0.008	0.011	0.002	0.005	0.000	0.005	0.277	0.003	0.000
Mg	0.607	0.419	0.779	0.000	0.000	0.345	0.000	0.000	0.006
Zn	0.001	0.002	0.002	0.000	0.000	0.000	0.132	0.002	0.000
Ca	0.000	0.000	0.000	0.000	0.000	0.001	0.000	0.000	0.002
Sum^{2+}	1.021	0.999	1.006	1.001	1.982	0.902	0.987	0.226	0.190
$Sum^{3,4+}$	1.978	2.000	1.994	1.999	1.009	1.097	1.006	1.773	1.864
Total cations	3.000	3.000	3.000	3.000	2.991	2.000	1.994	2.000	2.053

Notes: LN_50 is from kimberlite pipe no. 50 in LiaoNing province, P.R. China, HB is from a spinel-lherzolite in Hebei province, P.R. China.
* Samples no. 84, no. 497, no. 20 are from P. R. China, the specific localities are unknown.
† HMS3 analysis from Table 2 of Morris et al. (1985).
‡ Fe^{2+}/Fe^{3+} ratios were adjusted to optimize stoichiometry (cation sums = 3 for spinels 2 for ilmenite).

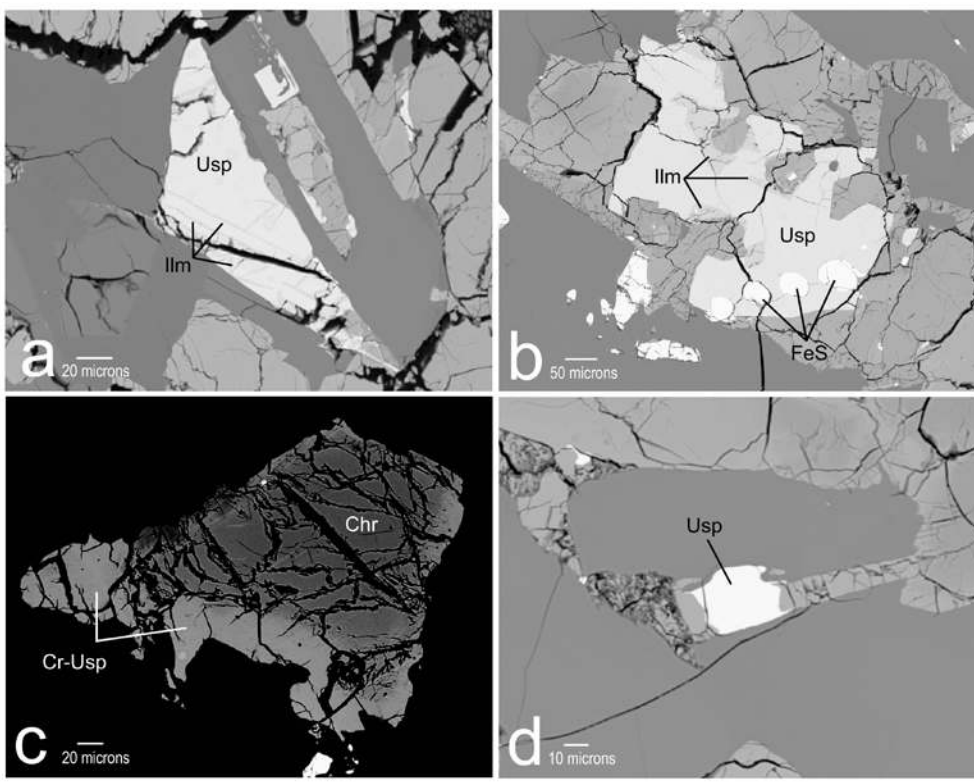

FIGURE 1. Backscattered electron images of oxides in EETA79001, 357 = lithology B (a and b) and EETA79001,442 = lithology A (c and d). (a) Ulvöspinel with ilmenite intergrowths. (b) Ulvöspinel with blebs of iron sulfide and ilmenite intergrowths. (c) Cr-ulvöspinel overgrowth on a chromite xenocryst. (d) Groundmass ulvöspinel. Usp = ulvöspinel, Ilm = ilmenite, FeS = iron sulfide, Chr = chromite, and Cr-Usp = chromian ulvöspinel.

TABLE 2a. Average compositions of Fe-Ti-Cr oxides in EETA79001,442 by electron microprobe

	EETA79001,442 (lithology A)													
Phase	Al-Chromite		Al-Ti-Chromite		High Cr-ulvöspinel		Cr-ulvöspinel		Ulvöspinel		Titanomagnetite		Ilmenite	
No. analyses	ave. (n = 11)	sdev	ave. (n = 2)	sdev	ave. (n = 12)	sdev	ave. (n = 8)	sdev	ave. (n = 13)	sdev	ave. (n = 2)	sdev	ave. (n = 8)	sdev
FeO(t)	30.80	1.57	42.16	2.42	49.79	2.22	56.35	1.84	64.72	1.94	67.38	0.15	44.73	0.61
MgO	3.49	1.10	3.13	0.27	2.53	0.60	1.80	0.51	1.24	0.22	2.27	0.29	1.97	0.36
Cr_2O_3	53.29	0.97	34.28	3.68	21.99	2.50	9.92	2.27	1.96	1.56	4.60	0.07	0.25	0.09
TiO_2	0.77	0.17	10.33	3.16	17.19	1.49	22.53	2.08	26.16	1.75	15.09	0.01	51.69	0.41
MnO	0.43	0.03	0.43	0.03	0.54	0.04	0.58	0.06	0.60	0.05	0.62	0.03	0.64	0.04
V_2O_3	0.56	0.05	0.73	0.01	0.68	0.38	0.75	0.15	0.31	0.19	0.44	0.20	0.00	0.01
Al_2O_3	7.03	0.74	6.16	1.13	5.61	3.36	4.97	1.92	2.62	0.64	4.85	0.00	0.11	0.02
CaO	0.06	0.09	0.14	0.12	0.12	0.09	0.26	0.05	0.16	0.11	0.67	0.12	0.24	0.22
ZnO	0.07	0.06	0.18	0.14	0.05	0.05	0.06	0.07	0.04	0.04	0.06	0.05	0.02	0.02
SiO_2	0.21	0.21	0.13	0.02	0.04	0.03	0.13	0.06	0.06	0.03	1.94	1.01	0.05	0.02
Oxide Sum	96.7		97.7		98.6		97.4		97.9		97.9		99.7	
FeO	27.29		36.32		43.60		49.3		53.59		43.78		41.99	
Fe_2O_3	3.90		6.49		6.87		7.9		12.37		26.23		3.04	
Corr. Sum*	97.1		98.3		99.2		98.1		99.1		100.6		100.0	
Number of cations on the basis of 4 oxygen atoms for spinels, 3 for ilmenite and hematite														
Si	0.008	0.01	0.005	0.00	0.002	0.00	0.005	0.00	0.002	0.00	0.069	0.03	0.001	0.00
Al	0.299	0.03	0.261	0.05	0.236	0.14	0.214	0.08	0.114	0.03	0.204	0.00	0.003	0.00
Ti	0.021	0.00	0.279	0.08	0.465	0.05	0.620	0.06	0.726	0.05	0.405	0.01	0.967	0.00
V^{3+}	0.016	0.00	0.021	0.00	0.020	0.01	0.022	0.00	0.009	0.01	0.013	0.01	0.000	0.00
Cr	1.521	0.04	0.975	0.11	0.624	0.07	0.287	0.07	0.057	0.05	0.130	0.00	0.005	0.00
Fe^{3+}	0.108	0.01	0.176	0.01	0.189	0.03	0.229	0.06	0.365	0.09	0.706	0.04	0.057	0.01
Fe^{2+}	0.823	0.06	1.091	0.08	1.307	0.06	1.495	0.07	1.632	0.05	1.306	0.01	0.873	0.01
Mn^{2+}	0.013	0.00	0.013	0.00	0.017	0.00	0.018	0.00	0.019	0.00	0.019	0.00	0.014	0.00
Mg	0.187	0.06	0.168	0.01	0.135	0.03	0.098	0.03	0.068	0.01	0.121	0.01	0.073	0.01
Zn	0.002	0.00	0.005	0.00	0.001	0.00	0.002	0.00	0.001	0.00	0.002	0.00	0.000	0.00
Ca	0.002	0.00	0.005	0.00	0.005	0.00	0.010	0.00	0.006	0.00	0.026	0.00	0.007	0.01
Sum^{2+}	1.027		1.282		1.465		1.623		1.727		1.473		0.966	
$Sum^{3,4+}$	1.972		1.717		1.535		1.376		1.273		1.527		1.033	
Total cations	3.000		3.000		3.000		3.000		3.000		3.000		2.000	
% Mgt	0.05		0.09		0.09		0.12		0.18		0.38			
% Chr	0.76		0.49		0.31		0.15		0.03		0.07			
% Usp	0.02		0.28		0.47		0.63		0.73		0.43			
% Spinel	0.17		0.15		0.13		0.10		0.06		0.12			

* Fe^{2+}/Fe^{3+} ratios were adjusted to optimize stoichiometry (cation sums = 3 for spinels 2 for ilmenite).

TABLE 2b. Average compositions of Fe-Ti-Cr oxides in EETA79001,357 by electron microprobe

	EETA79001,357 (lithology B)									
Phase	Al-Chromite		Al-Ti-Chromite		High Cr-ulvöspinel		Cr-ulvöspinel	Ulvöspinel		Ilmenite	
no. analyses	ave. (n = 5)	sdev	ave. (n = 2)	sdev	ave. (n = 4)	sdev	ave. (n = 1)	ave. (n = 39)	sdev	ave. (n = 5)	sdev
FeO(t)	32.40	2.31	41.25	5.13	50.21	1.80	55.43	66.59	1.86	46.97	0.21
MgO	2.54	1.41	2.28	0.51	1.48	0.41	1.61	0.22	0.11	0.33	0.05
Cr_2O_3	53.81	2.30	37.35	5.87	25.05	2.73	10.92	0.68	0.77	0.02	0.03
TiO_2	1.24	0.31	7.08	4.44	15.97	1.34	24.07	26.69	1.74	52.13	0.41
MnO	0.44	0.03	0.41a	0.03	0.49	0.04	0.55	0.60	0.05	0.63	0.03
V_2O_3	0.92	0.10	0.88	0.05	0.84	0.13	0.90	0.24	0.21	0.00	0.00
Al_2O_3	7.47	1.46	9.25	3.07	4.21	0.68	3.60	2.15	0.78	0.06	0.02
CaO	0.10	0.10	0.14	0.09	0.12	0.08	0.17	0.14	0.20	0.04	0.04
ZnO	0.03	0.01	0.08	0.00	0.07	0.13	0.14	0.08	0.06	0.04	0.05
SiO_2	0.08	0.02	0.05	0.03	0.04	0.02	0.07	0.13	0.21	0.06	0.02
Oxide Sum	99.0		98.8		98.5		97.5	97.5		100.3	
FeO	29.84		35.54		43.83		50.31	55.21		45.65	
Fe_2O_3	2.84		6.34		7.09		5.69	12.64		1.47	
Corr. Sum*	99.3		99.4		99.2		98.0	98.8		100.4	
Number of cations on the basis of 4 oxygen atoms for spinels, 3 for ilmenite and hematite											
Si	0.003	0.00	0.002	0.00	0.002	0.00	0.003	0.005	0.01	0.002	0.00
Al	0.312	0.05	0.384	0.12	0.181	0.03	0.157	0.095	0.03	0.002	0.00
Ti	0.033	0.01	0.189	0.12	0.438	0.04	0.668	0.751	0.04	0.983	0.00
V^{3+}	0.026	0.00	0.025	0.00	0.025	0.00	0.027	0.007	0.01	0.000	0.00
Cr	1.511	0.08	1.041	0.15	0.721	0.07	0.319	0.020	0.02	0.000	0.00
Fe^{3+}	0.080	0.03	0.169	0.03	0.195	0.02	0.158	0.368	0.07	0.030	0.01
Fe^{2+}	0.883	0.07	1.051	0.15	1.336	0.06	1.553	1.715	0.05	0.955	0.01
Mn^{2+}	0.013	0.00	0.012	0.00	0.015	0.00	0.017	0.019	0.00	0.013	0.00
Mg	0.133	0.07	0.120	0.02	0.080	0.02	0.089	0.012	0.01	0.012	0.00
Zn	0.001	0.00	0.002	0.00	0.002	0.00	0.004	0.002	0.00	0.001	0.00
Ca	0.004	0.00	0.005	0.00	0.005	0.00	0.007	0.006	0.01	0.001	0.00
Sum^{2+}	1.034		1.190		1.438		1.669	1.754		0.983	
$Sum^{3,4+}$	1.965		1.810		1.561		1.330	1.245		1.016	
Total cations	3.000		3.000		3.000		3.000	3.000		2.000	
% Mgt	0.04		0.09		0.10		0.08	0.19			
% Chr	0.78		0.55		0.37		0.16	0.01			
% Usp	0.03		0.20		0.45		0.67	0.77			
% Spinel	0.15		0.16		0.09		0.08	0.03			

* Fe^{2+}/Fe^{3+} ratios were adjusted to optimize stoichiometry (cation sums = 3 for spinels 2 for ilmenite).

1986; Wang et al. 2001c). There are, however, a detailed Raman study on Mg-Fe-Cr-Al spinels (Malézieux and Piriou 1988), and detailed polarization Raman studies on Fe_2O_3 (Beattie and Gilson 1970) and Fe_3O_4 (Gasparov et al. 2000). We are unaware of previous Raman studies of ulvöspinel (Fe_2TiO_4), ilmenite ($FeTiO_3$), and the related solid solutions (Fe_3O_4-Fe_2TiO_4, Fe_2O_3-$FeTiO_3$).

Most Fe-Ti-Cr-oxides produce weaker Raman signals than those from oxyanionic minerals and Ti or Al oxides. This difference is partly because the dark colors of the Fe-oxides limit the penetration depth of the excitation laser beam (visible wavelength) and of the produced Raman radiation, and partly because most Fe-oxides are intrinsically weaker Raman scatterers than the oxyanionic minerals. To first order, the intensity of the Raman signal from a mineral (a scatterer) is proportional to the fourth power of the excitation laser frequency, the concentration of the scatterer in the sample, and the second power of the average polarizability of the scatterer. The major factors that influence the strength of the Raman signal of a mineral are the rigidity of the polyhedra in its structure [indicated by the bulk modulus (Brout 1959; Hofmeister 1991)] and the degree of covalency of its chemical bonds. Differences in electronegativity between elements in a chemical bond are commonly used to estimate the degree of covalency of a chemical bond. For example (Emsley 1993), the degree of covalency in Fe-Oxides is only ~30–44%, compared to ~54% in the $(SiO_4)^{4-}$ units of silicates, ~66% in the $(PO_4)^{3-}$ unit of phosphates, and ~80% for the C-O and S-O bonds in carbonates and sulfates. Furthermore, the strongest peak in the Raman spectrum of a mineral is generated by the bond having the highest degree of covalency. The main Raman peaks of silicates are thus generated by SiO_4 units and their polymers, and the Fe-, Mg-, Ca-, Mn-O bonds in those minerals typically produce much weaker spectral features. In the Raman spectra of Fe-oxides, the differences in bond strength between different types of polyhedra (e.g., FeO_4 tetrahedra and CrO_6 octahedra in chromite) are less pronounced than those in oxyanionic minerals (e.g., MgO_6 octahedra and CO_3 groups in magnesite), so only approximate "major contributors" to the Raman spectral features can be assigned for Fe-oxides. Moreover, the role of "major contributor" can be changed by cation substitutions, which can cause a change of spectral pattern. In Table 3, the suspected major contributors of the Raman features are marked in bold typeface for the Fe-Ti-Cr-oxides discussed in this paper.

In the following section, we discuss the Raman spectral features of each mineral group and their dependences on chemistry and structure, on the basis of co-registered Raman and EMP data taken from individual Fe-Ti-Cr oxide samples and those found in thin sections (TS442 and TS357) of EETA79001. This information will be used in the last section to analyze the Raman point-count data from the rock chips of EETA79001 as a simulation of planetary on-surface investigations.

Experimental results and discussion

Chromite group – correlation between Raman peak positions and chemistry

Chromite has a normal spinel structure and belongs to the Fd3m space group (O_h^7 point group), with two formula units $[^{IV}(Fe^{2+}, Mg^{2+})\ ^{VI}(Cr^{3+}, Fe^{3+}, Al^{3+})_2O_4]$ in a primitive unit cell. The normal spinel structure consists of a cubic close-packed array of oxygen atoms with trivalent cations occupying half of the octahedral interstices and divalent cations occupying one eighth of the tetrahedral interstices. Factor-group analysis suggests that five Raman-active vibrational modes are allowable for oxide spinels, with the following symmetries: $A_{1g} + E_g + 3F_{2g}$ (Chopelas and Hofmeister 1991). The Raman spectral pattern of end-member chromite (Fig. 2) consists of a major broad peak near 685 cm^{-1} and a shoulder near 650 cm^{-1}. Other minor peaks are seen near ~610, ~520, and ~450 cm^{-1}. The strongest peak, ~685 cm^{-1}, was assigned to the A_{1g} mode by Malézieux and Piriou (1988); this feature presumably is generated by the bonds in $(Cr^{3+}, Fe^{3+}, Al^{3+})O_6$ octahedra (Table 3). The trivalent ions lead to a more compact structure and a higher degree of covalency than those in $Fe^{2+}O_4$ tetrahedra. On the basis of peak assignments in numerous Raman studies of different spinels (Table 4, Chopelas and Hofmeister 1991; Cynn et al. 1992; Busey and Keller 1964; McMillan and Akaogi 1987; Yamanaka and Ishii 1986; Ross and Navrotsky 1987; White and DeAngelis 1967; Degiorgi et al. 1987; Gasparov et al. 2000), we infer that the peak near 650

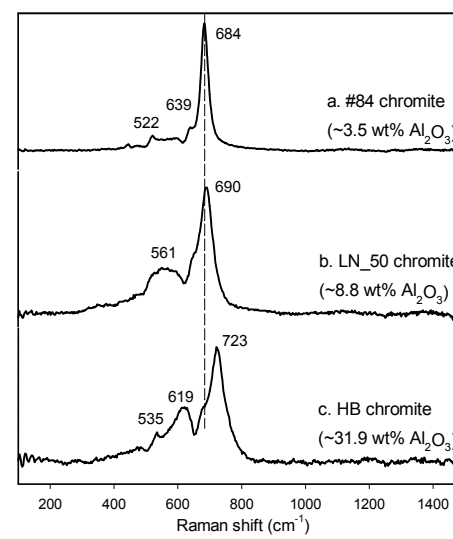

Figure 2. Raman spectra of three chromite-spinel solid-solution samples.

Table 3. Chemistries, structures, & site occupancies of minerals in this study

Structure	Normal spinel		Inverse spinel			Corundum	Pseudo-corundum
Minerals	Chromite	Ulvöspinel	Solid solution		Magnetite	Hematite	Ilmenite
Formula	$(Mg,Fe)(Cr,Al,Fe)_2O_4$	$Fe_2^{2+}Ti^{4+}O_4$	$Usp_{0.8}Mgt_{0.2}$	$Usp_{0.2}Mgt_{0.8}$	$Fe_2^{3+}Fe^{2+}O_4$	α-Fe_2O_3	$FeTiO_3$
Space group			$O_h^7 - Fd3m$			$D_{3d}^6 - R\bar{3}C$	$C_{3i}^2 - R\bar{3}$
Vib. modes			$A_{1g} + E_g + 3F_{2g}$			$2A_{1g} + 5E_g$	$5A_g + 5E_g$
Octahedra	**$Cr^{3+}O_6$, $Al^{3+}O_6$, $Fe^{3+}O_6$**	**$Ti^{4+}O_6$**, $Fe^{2+}O_6$	**$Ti^{4+}O_6$**, $Fe^{2+}O_6$	**$Ti^{4+}O_6$, $Fe^{3+}O_6$**, $Fe^{2+}O_6$	**$Fe^{3+}O_6$**, $Fe^{2+}O_6$	**$Fe^{3+}O_6$**	**$Ti^{4+}O_6$**
Tetrahedra	$Mg^{2+}O_4$, $Fe^{2+}O_4$	$Fe^{2+}O_4$	$Fe^{2+}O_4$, $Fe_{3+}O_4$	$Fe^{3+}O_4$	$Fe^{3+}O_4$		$Fe^{2+}O_6$, $Mg^{2+}O_6$

Notes: The ionic groups in bold are the suggested major contributors of the Raman spectral features of these Fe-Ti-Cr-oxides.

TABLE 4. Raman peaks and their assignments for minerals of spinel structure

Minerals	Spinel (syn.)	Spinel (nat.)						Gahnite	Magnetite (130K)	Magnetite	Magnetite	Ulvöspinel	Chromite
Formula	$MgAl_2O_4$	$MgAl_2O_4$	Na_2MoO_4	Na_2WO_4	γ-Mg_2SiO_4	γ-Ni_2SiO_4	γ-Mg_2GeO_4	$ZnAl_2O_4$	$Fe^{2+}Fe^{3+}{}_2O_4$	$Fe^{2+}Fe^{3+}{}_2O_4$	$Fe^{2+}Fe^{3+}{}_2O_4$	Fe_2TiO_4	$FeCr_2O_4$
A_{1g} (v_1)	767m	770m	892	928	794s	849s	669s	758w	672s	670s	667s	680s	690s
E_g (v_2)	407s	409s	381	373	370w	369s	341w	417s					520m
F_{2g} (v_3)	312m	311m	808	813	836m	810m	777s	196w	318m	308m	305w		600w
F_{2g} (v_4)	666m	670m	303	312	600w	675w	520w	509w	542m	540m	539w	497m	650w
F_{2g} (trans.)	492w		116	93	302w	190w	213w	658s	410w	193w			445w
Add. peaks		727w										561m	
Data from	1	2	3	3	4	4, 5	6	1	8	9	10	10	10
Peak assigned by	1	2	7	7	4	5	10	1	8	9	10	10	10

Notes: vs = very strong, s = strong, m = middle, w = weak, vw = very weak; 1. = Chopelas and Hofmeister 1991; 2 = Cynn et al. 1992; 3 = Busey & Keller 1964 ; 4 = McMillan & Akaogi 1987; 5 = Yamanaka & Ishii 1986; 6 = Ross & Navrotsky 1987; 7 = White & DeAngelis, 1967; 8 = Degiorgi et al. 1987; 9 = Gasparov et al. 2000; 10 = this study.

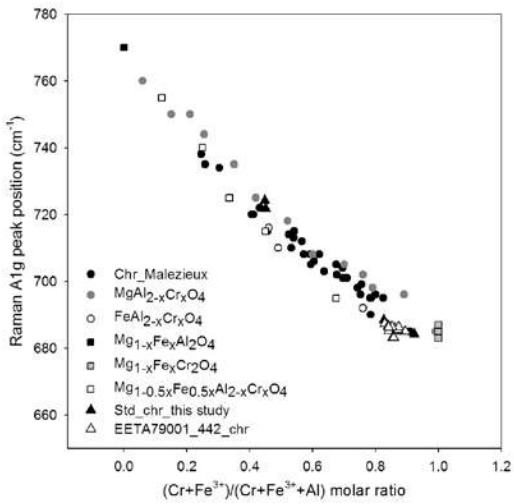

FIGURE 3. Correlation between the Raman A_{1g} peak position of chromite-spinel solid solutions and the molar ratio $(Cr + Fe^{3+})/(Cr + Fe^{3+} + Al)$ on the basis of data from this study and the data of Malézieux and Piriou (1988).

cm^{-1} in the chromite spectrum belongs to F_{2g} symmetry, and other minor peaks to E_g and F_{2g} symmetries.

Compositionally, Cr^{3+}, Al^{3+}, and Fe^{3+} in octahedral sites and Fe^{2+} and Mg^{2+} in tetrahedral sites in the spinel structure form complete solid solutions. In nature, "chromite" covers a wide range of solid solutions containing Cr^{3+}, Al^{3+}, Fe^{3+}, Fe^{2+}, Mg^{2+}, and trace amounts of Zn^{2+}, Mn^{2+}, Ti^{4+}, and other minor cations. Cation substitution in chromite causes various changes in the Raman spectral pattern. Malézieux et al. (1983) observed the appearance of a shoulder near 735 cm^{-1} as the Cr_2O_3 concentration rose above 63 wt%. Some mantle-derived chromites (inclusions in diamond) of similar compositions (Cr_2O_3 >63 wt%) yield their strongest peak at an abnormally high wavenumber of ~730 cm^{-1} (Wang et al. 1994). In contrast to the five predicted Raman active modes for the spinel structure, high-Cr chromites show weak shoulders around their major Raman peaks as well as in their IR spectra. It has been suggested that local distortions around the trivalent cations cause a symmetry change from D_{3d} to C_{3v} and a crystal structure change from O_h^7 to T_d^2, which increases the total number of Raman (and IR) active modes from five to seven (Grimes and Collett 1971).

Cation substitution also causes Raman peak positions to shift over a substantial spectral range. The Raman spectra of the three chromite samples in Figure 2 show a ~40 cm^{-1} shift in the peak position of the A_{1g} mode, and changes in peak pattern owing to shifts in the positions of the minor peaks. The correlation between the A_{1g} peak position and the chemical composition of chromite was studied in detail by Malézieux et al. (1980, 1983, 1986, 1988), who used five series of 27 synthetic samples ($MgAl_{2-x}Cr_xO_4$, $FeAl_{2-x}Cr_xO_4$, $Mg_{1-x}FeAl_2O_4$, $Mg_{1-x}Fe_xCr_2O_4$, $Mg_{1-x/2}Fe_{x/2}Al_{2-x}Cr_xO_4$) and 33 natural chromite samples. They observed a continuous frequency shift of the A_{1g} mode following the cation substitution in octahedral sites from 770 cm^{-1} ($MgAl_2O_4$) to 683 cm^{-1} ($Mg_{0.7}Fe_{0.3}Cr_2O_4$), which can be expressed as a polynomial function of the cation ratio $(Cr + Fe^{3+})/(Cr + Al + Fe^{3+})$ (Fig. 3). The peak arising from the A_{1g} mode in the first spectrum of Figure 2 is significantly narrower than those of the other two spectra. No obvious degradation of crystal symmetry or structural change was observed, except for a systematic shift in peak position to higher wavenumbers and a broadened peak of the A_{1g} mode as the result of increasing the proportion of $Al^{3+}O_6$ (Table 3). This result suggests that substitution of Cr^{3+} and Fe^{3+} by Al^{3+} in octahedral sites is random, resulting in a disordered cation distribution.

Five individual chromite and chromite-spinel solid solution grains were measured by Raman spectroscopy and electron probe microanalysis on the same sample spots. The A_{1g} peak positions of these chromite grains demonstrate systematic shifts according to their compositions (Table 1). These data fall on the same trend and have uncertainties similar to the 60 chromite samples in the study of Malézieux and Piriou (1988), shown as a function of $(Cr + Fe^{3+})/(Cr + Fe^{3+} + Al)$ in octahedral sites in Figure 3. This finding further supports the interpretation that the vibration of the $A^{3+}O_6$ ($A = Al^{3+}$, Cr^{3+}, Fe^{3+}) octahedron is the major contributor to the main Raman peak of chromite (Table 3). No obvious correlation was found between the A_{1g} peak position and $Fe^{2+}/(Fe^{2+} + Mg)$ in tetrahedral sites of these samples (see Fig. 2 in Wang et al. 2001c). The large range in variation (~100 cm^{-1}) of A_{1g} peak shifts is caused mainly by the difference in atomic mass of Al^{3+} compared with those of $Cr^{3+}$and Fe^{3+} (mass difference Δm ~25–29 units). Using this correlation, compositional information on chromite can be extracted from its major Raman peak position, even if the S/N is low, as in a rock sample.

Seven xenocrystic grains found in thin section TS442 of EETA79001 (lithology A) are zoned (c in Fig. 1), with central cores of average composition $(Mg_{0.20}Fe^{2+}_{0.83})(Cr_{1.59}Ti_{0.02}Fe^{3+}_{0.04}Al^{3+}_{0.28})O_4$, and rims of average composition $(Mg_{0.15}Fe^{2+}_{0.83})(Cr_{0.76}Ti_{0.45}Fe^{3+}_{0.14}Fe^{2+}_{0.46}Al^{3+}_{0.18})O_4$. These compositions are sufficiently different from each other that Raman spectra from the cores

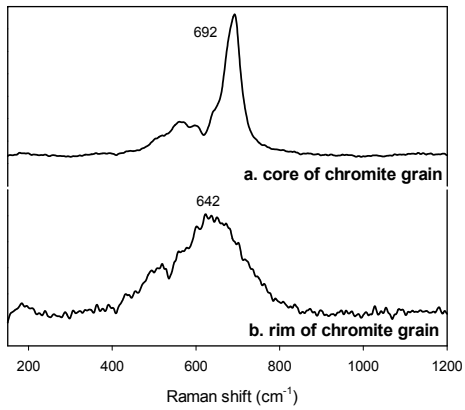

FIGURE 4. Raman spectra from the core (chromite) and the rim (Cr-ulvöspinel) of a chromite xenocryst in EETA79001, 442 thin section.

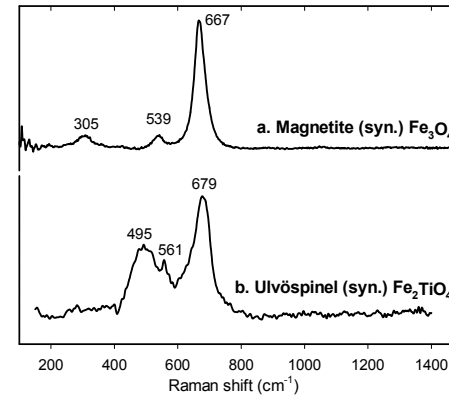

FIGURE 5. Raman spectra of synthetic end-member magnetite and ulvöspinel.

and rims of the grains have different spectral patterns (Fig. 4). The major Raman peak positions obtained by curve fitting of the spectra from the cores of different chromite grains range from 690.8 cm^{-1} to 692.8 cm^{-1}. Using the correlation in Figure 3, these Raman peak positions suggest $(Cr + Fe^{3+})/(Cr + Fe^{3+} + Al)$ values of 0.75–0.93. This range is consistent with the heterogeneous compositions revealed by EMP analyses, but the range extends slightly beyond the range (0.83–0.87) determined by EMP analyses. The broader range for the Raman compositions occurs because the EMP data were taken strictly on the cores of the mineral grains, but the Raman data include some zoned portions. This situation occurs partly because the diameter of the laser beam exceeds that of the electron beam and partly because the imaging used to place the Raman beam does not distinguish between core and zoned compositions. For both reasons, the Raman instrument encounters a greater range of compositions than the EMP. The spectral pattern from the rims of these chromite grains (Cr-ulvöspinel) will be discussed in the next section.

Ulvöspinel, magnetite, and their solid-solutions Usp-Mgt_{ss}

Both ulvöspinel (Fe_2TiO_4) and magnetite ($FeFe_2O_4$) have inverse spinel structures (Hill et al. 1979). In magnetite, $[^{IV}(Fe^{3+})^{VI}(Fe^{2+}Fe^{3+})O_4]$, half of the Fe^{3+} occurs in tetrahedral sites and the other half of the Fe^{3+} and all of the Fe^{2+} occur in octahedral sites. In the structure of ulvöspinel, $[^{VI}(Fe^{2+})^{IV}(Fe^{2+}Ti^{4+})O_4]$, half of the Fe^{2+} occurs in tetrahedral sites and the other half of the Fe^{2+} and all Ti^{4+} occurs in the octahedral sites. The inverse spinel structure has the same space group, $Fd3m$-O_h^7, as the normal spinel structure (Hill et al. 1979) and thus has the same number of Raman active vibrational modes $A_{1g} + E_g + 3F_{2g}$ (Table 3). We have found no published Raman studies on ulvöspinel. Figure 5 shows the Raman spectra of magnetite and ulvöspinel taken on synthetic end-member samples.

The major peak of a synthetic end-member magnetite (sample from Finger et al. 1986) occurs at 667 cm^{-1} (Fig. 5a), along with two minor peaks at 539 and 305 cm^{-1}. The vibrations of Fe^{3+}-O bonds in both octahedra and tetrahedra should be the main contributors because of their higher degree of covalency than Fe^{2+}-O bonds (Table 3). On the basis of a polarization Raman study (Gasparov et al. 2000), it appears that the major peak at 667 cm^{-1} can be assigned to A_{1g} symmetry and the two minor peaks to F_{2g} symmetry. There are small differences between the values of Raman peak positions reported in this study and those in the literature (Table 4). In one of these studies (Degiorgi et al. 1987), the spectrum was recorded at 130K. The Raman peak positions of magnetite (especially A_{1g} mode) vary slightly with temperature (300 to 40K) as reported by these two studies. At room temperature, the A_{1g} peak of magnetite is ~17 cm^{-1} lower than the 684 cm^{-1} peak of a chromite of $[(Fe_{0.52}Mg_{0.47})(Cr_{1.83}Al_{0.14}Fe_{0.02})O_4)]$. The mass effect of the lighter cations Al^{3+} and Cr^{3+} in octahedral sites of chromite, compared to Fe^{3+} in magnetite, is the major cause of this difference in peak position.

The Raman spectrum of a synthetic end-member ulvöspinel (Fig. 5b, sample from Wechsler et al. 1984, USP100–1200, well-crystallized Fe_2TiO_4 with ≤2 wt% ilmenite identified by XRD) has its strongest peak at 679 cm^{-1}; the peak is broader than the major peak of magnetite (Fig. 5a). A secondary peak of ulvöspinel occurs near 495 cm^{-1} and it is much stronger (~50% the intensity of the major peak) and broader than the secondary peaks of chromite and magnetite (which are only 10–30% as intense as the major peaks). A sharp peak at ~561 cm^{-1} occurs between the two strong peaks of ulvöspinel; it is a characteristic peak that can be used to distinguish ulvöspinel from other Fe-Ti oxides. Spectral curve fitting suggests that another peak occurs as a shoulder (~610 cm^{-1}) on the wing of the major peak. Following the same principle used for chromite, we suggest that $Ti^{4+}O_6$ octahedra should be the major producer of the main Raman peak of ulvöspinel (Table 3).

The Raman peaks of our end-member ulvöspinel sample are substantially broader than those of end-member chromite and magnetite. Compositional peak broadening of the type described above for some chromites (Fig. 2b and 2c) cannot be the reason, however. Structural data (Smyth and Bish 1988) suggest that ulvöspinel is similar to chromite in the extent of its octahedral distortions. Both chromite and ulvöspinel have larger central polyhedral angular distortions than magnetite (31.6 and 46.7° compared to 5.6° for magnetite), and both show extensive quadratic elongation (Q. E. ~ 1.0084 and 1.0123 compared to 1.0015 for magnetite; Q. E. is unitless and defined by Robinson et al. 1971). We would expect ulvöspinel and chromite to have similar

peak widths if these structural distortions were the cause. If not, then the reason for the wider peaks of the ulvöspinel shown in Figure 5b (compared to the magnetite of Fig. 5a and the chromite of Fig. 2a) would be a property inherent to our particular sample. Unlike the single-crystal magnetite and chromite samples, our ulvöspinel sample is polycrystalline (grain size ~4–20 μm based on microscopic observations). Also, the sample was readily oxidized during analysis using ~9 mW laser power in an oxygen-rich atmosphere. This result suggests poor crystallinity, i.e., low translational symmetry or lack of long-range order. Small variations in bond lengths and bond angles among structural units in a poorly crystalline material can result in a range of vibrational frequencies, and so could broaden the spectral peaks.

Because ulvöspinel and magnetite both have an $Fd3m$–O_h^7 space group and inverse spinel structure, there is no structural change along the solid-solution series. The spectral variations come mainly from the different degrees of cation substitution. Magnetite and ulvöspinel form a complete solid solution (Usp-Mgt_{ss}, $Ti_xFe_{3-x}O_4$) at high temperature (e.g., 1300 °C). There is a miscibility gap at low temperature (600 °C) and the consolute point lies closer to Fe_3O_4 than to Fe_2TiO_4 (Lindsley 1991). Three models (Neel 1955; Chevallier et al.1955; Akimoto 1954; O'Reilly and Banerjee 1965) have been used to predict the distribution of Fe^{2+}, Fe^{3+}, and Ti^{4+} among the octahedral and tetrahedral sites when an additional Fe cation enters the structure of ulvöspinel. The combination model of O'Reilly and Banerjee (1965) seems to fit experimental data best (see Lindsley 1976). It uses the Neel model (Neel 1955) for the two compositional extremes, $0 \le x \le 0.2$ and $0.8 < x < 1.0$ and the Akimoto model (Akimoto 1954) for the region $0.2 \le x \le 0.8$ (x = no. of Ti cations or mol fraction of ulvöspinel). Using the cation distribution derived from this combination model and our understanding as described in Table 3, the main source of the Raman peaks of Usp-Mgt_{ss} would be the vibrations from $Ti^{4+}O_6$, $Fe^{3+}O_6$, and $Fe^{3+}O_4$ when $x < 0.8$, and those from $Ti^{4+}O_6$ and $Fe^{3+}O_4$ when $x > 0.8$ (Table 3). With more vibrational units than just $Ti^{4+}O_6$ contributing to the Raman spectrum, Raman spectral peaks of Usp-Mgt_{ss} would be wider than those of end-member magnetite and ulvöspinel, and with a higher degree of overlap of different peaks.

Ulvöspinel, titanomagnetite, Al-Cr-ulvöspinel-magnetite solid solutions, along with spinel-chromite solid solutions, have been identified in thin sections and in small rock chips of Martian meteorite EETA79001. Tables 2a and 2b lists the average compositions of each type. The distributions of these compositions are presented in the two ternary diagrams of Figure 6. Although they all have $Fd3m$ space group, those near end-member spinel and chromite would have a normal spinel structure, and those near end-member magnetite and ulvöspinel would have an inverse spinel structure. The Chr-Mgt-Usp diagram (Fig. 6a) shows two trends of essentially two-component solid solutions, Usp-Mgt_{ss} and Usp-Chr_{ss}. The Chr-Spn-Usp diagram (Fig. 6b) suggests another trend of two-component solid solution, $^2Chr_{77–87}$-$Spn_{13–23}$, and modifies the Usp-Chr_{ss} to be a more complex four-component solid solution Usp-Chr-Spn-Mgt_{ss}.

The plot shown in Fig. 6c, Mg/(Mg + Fe^{2+}) vs. Cr/(Cr + 2Ti) is a projection along one side of the "spinel prism" and represents variation of Mg/Fe^{2+} with Cr/Ti. This plot shows that the oxides in EETA79001 are iron rich and that they lie largely along an ulvöspinel-chromite mixing line. Magnesium correlates positively with Al, thus we represent its abundance through the spinel ($MgAl_2O_4$) component (Fig. 6b). Aluminum also correlates positively with Cr. In general, the chromite compositions that

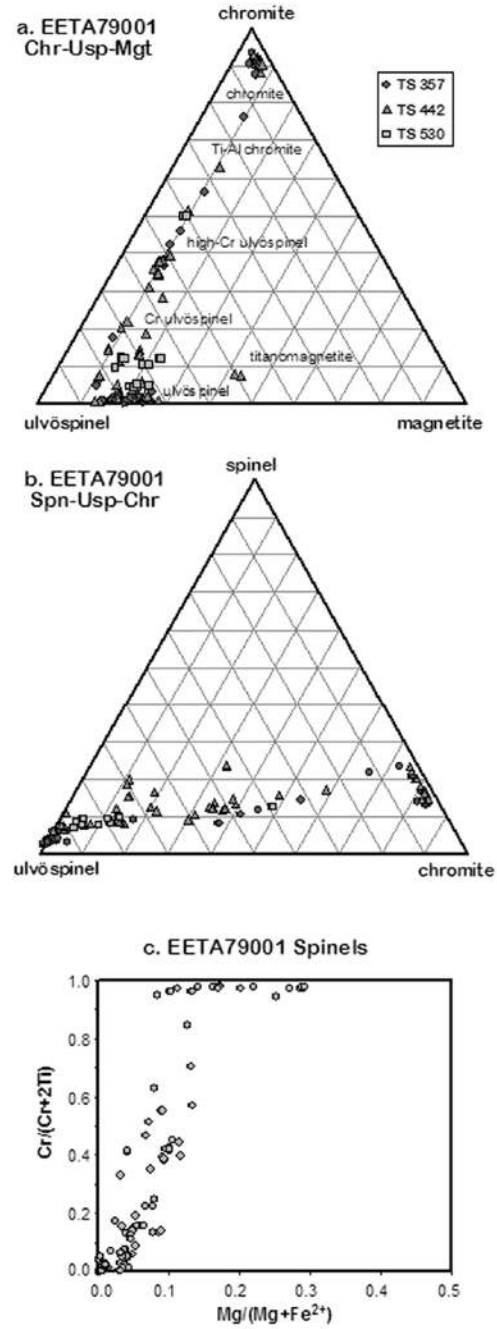

FIGURE 6. Ternary representations of oxide compositions in EETA79001. Thin section (TS) 357 is from Lithology B and TS 442 and 530 are from Lithology A. (**a**) Projection from spinel. Labels indicate nomenclature followed in text. (**b**) Projection from magnetite. Magnetite-$FeFe_2O_4$; ulvöspinel-Fe_2TiO_4; chromite-$FeCr_2O_4$; spinel-$MgAl_2O_4$. **(c)** Rectangular portion of "spinel prism" showing coupled variation of Mg/(Mg + Fe^{2+}) and Cr/(Cr + 2Ti) (atomic), which reflects variation of Mg/Fe along the chromite-ulvöspinel series.

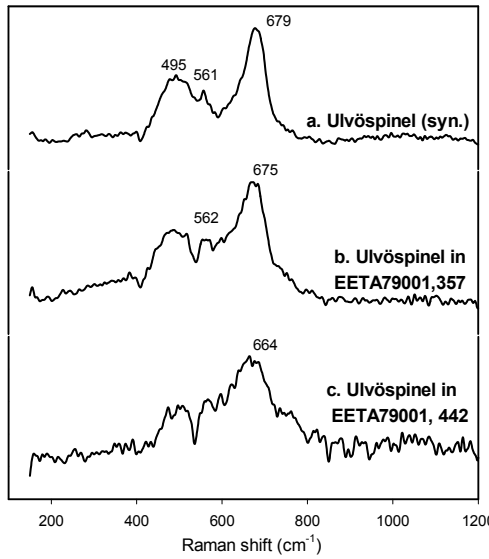

FIGURE 7. Raman spectra of ulvöspinel in EETA79001, 357 and EETA79001, 442 compared with that of end-member ulvöspinel.

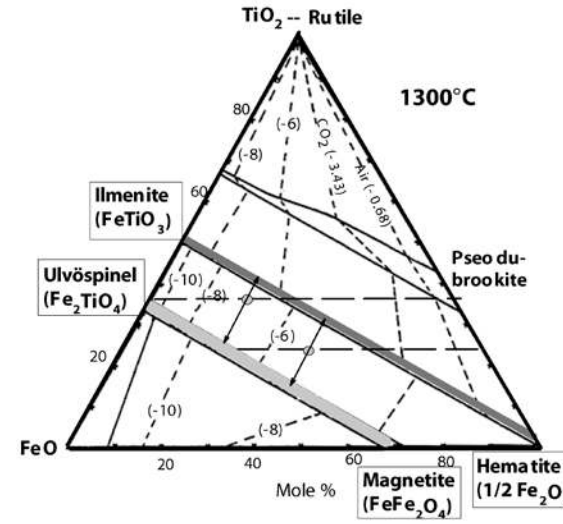

FIGURE 8. Phase relations for the system Fe-Fe_2O_3-TiO_2 at 1300 ºC and 1 atm total pressure (from Lindsley 1991). The light dashed lines represent oxygen isobars; values in parentheses are log f_{O_2}. The dark gray zone notates the solid solution field for Ilm-Hem_{ss}, and light gray zone for Usp-Mgt_{ss}. The uncolored zone in the middle of them is a two-phase field where Ilm-Hem_{ss} and Usp-Mgt_{ss} co-exist. Two horizontal heavy dashed lines from the end-member ulvöspinel and from an Usp-Mgt_{ss} indicate the paths taken during oxidation with constant Fe/Ti. The gray circle (on each path) marks the composition of possible oxidation product when the system reaches equilibrium at a certain f_{O_2}. This composition can be represented by the addition of two solid solutions, Ilm-Hem_{ss} and Usp-Mgt_{ss}, whose compositions are marked by the two-arrow-ends of the straight line that going through the gray circle.

have the highest Al concentrations also have the highest Mg/(Mg + Fe) values. This is consistent with their formation early in the crystallization sequence (McSween and Jarosewich 1983), similarly to lunar spinels (Papike et al. 1998). The Mg contents may also be high in part as a result of subsolidus equilibration with Mg-rich olivine (El Goresy 1976). The more Fe-rich ulvöspinel compositions have lower Mg/(Mg + Fe), consistent with formation late in the sequence. The systematics shown in Figure 6c are consistent with the association of chromite with magnesian olivine-orthopyroxene xenocrysts, and the intermediate Ti-Al chromite and chromian ulvöspinel compositions suggest a sequence of crystallization that is consistent with general trends in shergottite basalts and lherzolitic shergottites as summarized by McSween and Treiman (1998).

The Raman features of Chr-Spn solid solutions are compared in Figure 2. The spectral data from Chr-Spn solid solutions in EETA79001 are presented in Figure 3 and discussed in the previous section using the correlation developed based on our standard samples and those in the studies of Malézieux. Figure 7 compares the Raman spectrum of end-member ulvöspinel (Fig. 7a) with those from Usp-Mgt solid solutions and from more complex Usp-Chr-Spn-Mgt solid solutions in Martian meteorite EETA79001. The spectrum (Fig. 7b) from an Usp-Mgt solid solution ($Mgt_{0.19}Usp_{0.76}$, as averaged with other similar grains, Table 2b) in TS357 (lithology B) shows a typical ulvöspinel spectral pattern, with a central sharp peak appearing near ~562 cm^{-1} (Fig.7b). Curve-fitting of the spectra of similar grains reveals their major Raman A_{1g} peak position to be in the range of 667.4–670.7 cm^{-1}, ~9–12 cm^{-1} lower than the 679.5 cm^{-1} of end-member ulvöspinel. This downward shift correlates with the substitution of Ti^{4+} in the structure by heavier Fe, as well as with the general increase in Fe concentration. The positions of the secondary peaks are almost unchanged. Curve-fitting calculations also reveal broadening of the major peak (~675 cm^{-1}) and one secondary peak (~494 cm^{-1}) of these grains by ~50% and 12%, respectively, compared to end-member ulvöspinel. The peak shifts and broadening are presumably caused by contributions from additional vibrational units ($Fe^{3+}O_4$ and $Fe^{3+}O_6$), instead of only the $Ti^{4+}O_6$ in end-member ulvöspinel (Table 3). If that is the case, a continuous downward shift of the major Raman peak would be observed along with the oxidation of end-member ulvöspinel.

The phase relations of the system FeO-Fe_2O_3-TiO_2 at 1300 °C (Fig. 8, after Lindsley 1991) show that the oxidation products of ulvöspinel would have bulk compositions lying along the line from Fe_2TiO_4 (ulvöspinel) to Fe_2TiO_5 (pseudobrookite) (bold dashed line in Fig. 8), because no change in the ratio Fe/Ti should occur simply as a result of the oxidation. The mineral produced by this oxidation would be an ilmenite-hematite solid solution (Ilm-Hem_{ss}, $Fe_{2-x}Ti_xO_3$, $x > 0.6$) and an ulvöspinel-magnetite solid solution (Usp-Mgt_{ss}, $Fe_yTi_{3-y}O_4$) (indicated by the two arrow-ends of a solid line going through the upper gray circle), in which the values of x and y depend on the oxygen fugacity and the temperature during oxidation. This being so, a correlation can reasonably be sought between the Raman peak positions of one solid solution (e.g., Usp-Mgt_{ss}) and the ratio of the Raman peak areas of the two solid solutions (their relative proportions). Figure 9 shows a set of spectra obtained from several sample spots on a grain of the synthetic ulvöspinel sample (USP100–1200) that were oxidized by laser heating in air in this study. We note that the major Usp-Mgt_{ss} peak shifts to lower wavenumbers (from

TABLE 5. Raman peaks and their assignments for minerals of corundum structure

Minerals	Corundum	Corundum	Hematite		Hematite
Formula	Al_2O_3	Al_2O_3	Fe_2O_3	Cr_2O_3	Fe_2O_3
A_{1g}	418vs	417s	226s	303m	226s
E_g	378s	378m	245w		245w
E_g	432w	430w	293s	351w	292s
E_g	451w	451w	298s	397w	301sh
E_g	578w	576w	413m	530w	411m
A_{1g}	645m	644m	500m	551s	497m
E_g	751m	750m	612m	609w	613m
Add. peak					1321m
Data from	1	2	3	3	4
Peak assigned by	4	2	3	3	4

Notes: vs = very strong, s = strong, m = middle, w = weak, vw = very weak; 1 = White 1974; 2 = Xu et al. 1995; 3 = Beattie & Gilson 1970; 4 = This study.

678 to 655 cm^{-1}) whereas the peak intensities of Ilm-Hem_{ss} at ~290 and ~220 cm^{-1} increase. There is a good correlation (R^2 = 0.92) between the ratio of the Ilm-Hem_{ss} peak areas to the Usp-Mgt_{ss} peak areas and the major peak position of Usp-Mgt_{ss} (inset of Fig. 9, peak area values were obtained using the curve fitting algorithm of Grams/32 AI software). This experiment also supports the dependence of the major Raman peak position of Usp-Mgt_{ss} on the Ti/Fe ratio as indicated by data from Usp-Mgt_{ss} in EETA79001 TS357, discussed above.

The Raman spectra taken from four-component spinel solid solutions in the groundmass of TS442 (lithology A) and TS357 (lithology B) vary considerably, both in spectral pattern and peak positions. Some have their main peaks (e.g., ~635 cm^{-1}) at much lower Raman shifts than that of end-member magnetite (667 cm^{-1}). A few have their main peak position (e.g., ~684 cm^{-1}) at higher Raman shifts than that of end-member ulvöspinel (678 cm^{-1}). In most cases, the major peak is much broader than that of any end-member spinel (chromite, magnetite, ulvöspinel, Figs. 2 and 5), and in some cases, there are overlaps with secondary peaks, as shown by a very different spectral pattern, for example, in Figure 7c. The intermediate Chr-Usp-Spn-Mgt spinel solid solutions have quite a wide compositional range (Fig. 6a); in view of the wide range of cation substitutions in these four-component compositions, we suggest that these compositions might involve an increase in the degree of cation disorder, especially among the octahedral sites, which would broaden the major Raman peaks. In addition, the chemically complex solid solutions (Chr-Spn-Usp-Mgt) would be expected to have a structural framework that is distorted relative to both the normal spinel (chromite-spinel) and inverse spinel (ulvöspinel-magnetite) structures. Shock associated with the impact that sent EETA79001 to Earth may also have contributed to the apparent structural disorder of some grains. The Raman spectra (Fig. 4b) taken from the rim of xenocrystic chromite in TS442 (lithology A) show spectral features similar to those of Chr-Spn-Usp-Mgt solid solutions in the groundmass, presumably owing to the same complex compositions (Table 2a). We conclude that the compositional and structural disorder is the major reason for the wide range of shift of Raman peak positions and the variations of Raman spectral patterns among this group of spinel grains.

Ilmenite, hematite, and their solid-solutions Ilm-Hem_{ss}

Hematite has a corundum structure, $R\bar{3}c$-D^6_{3d}, in which oxygen atoms form an hexagonal close-packed framework, and Fe^{3+} fills 2/3 of the octahedral sites. Factor group analysis suggests 7 Raman-active vibrational modes ($2A_{1g} + 5E_g$) for this structure (Table 3, White 1974; Xu et al. 1995; Beattie and Gilson 1970), and we observe all of them in our Raman spectra (Fig. 10a, Table 5). Peak assignments are based on polarized Raman measure-

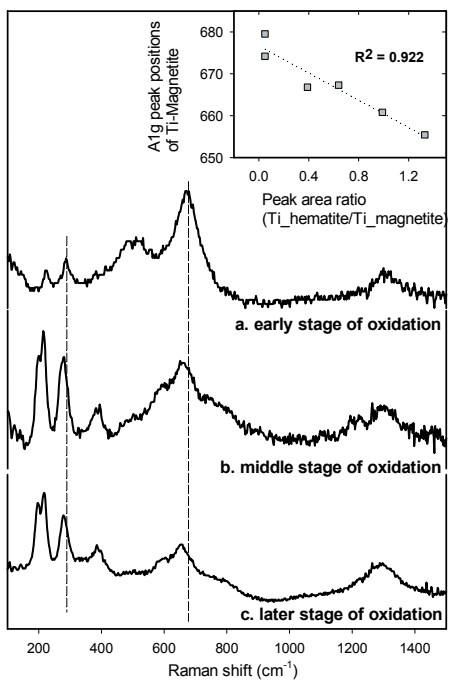

FIGURE 9. Raman spectra of oxidation products from an end-member ulvöspinel.

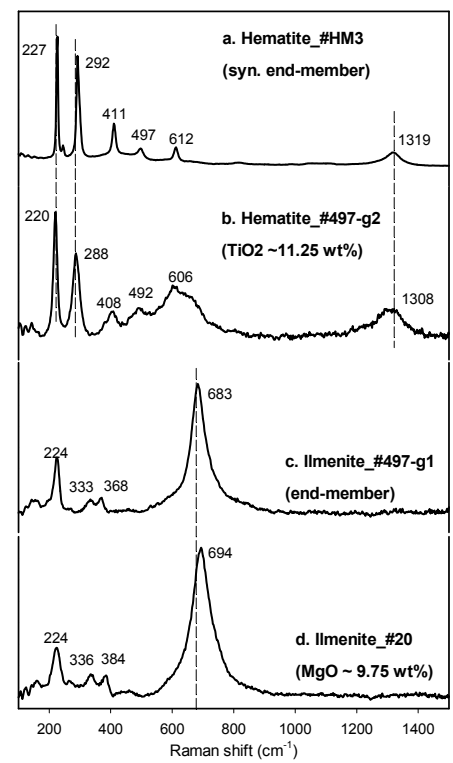

FIGURE 10. Raman spectra of ilmenite and hematite of variable compositions.

TABLE 6. Raman peaks and their assignments for minerals having ilmenite (pseudo-corundum) structure

Minerals	Geikielite	Geikielite	Geikielite	Pyrophanite	Pyrophanite									ilmenite
Formula	$MgTiO_3$	$MgTiO_3$	$MgTiO_3$	$MnTiO_3$	$MnTiO_3$	$LiNbO_3$	$NaNbO_3$	$ZnTiO_3$	$CdTiO_3$	$MgSiO_3$	$MgGeO_3$	$ZnSiO_3$	$ZnGeO_3$	$FeTiO_3$
A_g(1), X-O stretch	714s	710s	720s	685s	682	735vs	733vs	715s	700m	799vs	722vs	793s	718vs	683s
E_g(1), X-O stretch	641m		649m		599	677w	673w	620m	602m	683w	615w	666w	607w	
A_g(2), O-X-O bend	502sh		491m	461	468	470m	487s	472m	465m	620m	472m	595s	452m	
E_g(2), O-X-O bend	485m	483w					476sh	485sh			450m		445m	
E_g(3), O-X-O bend	397m		404m	359w	360	381w		395w		499sh		487s		
A_g(3) O-X-O bend	352vs	394m	359s	334vw	335	291m	287vs	345vs	325vs	480s	375w	474s	355w	
A_g(4), T(XO_6) translation	327s	349m	332s	259w	264		212s	267s	245s	412m	329w	348s	305m	368w
E_g(4), T(XO_6) translation	306w	325w	312w		235	275m	257m	233s	215s	399w	313m		214m	333w
A_g(5), T(M) translation	281vs		287s		202	214m	202s	179s	143s	346m	265w	199s	188m	270w
E_g(5), T(M) translation	224m	227m	230w		168	173w	163m	146s		287w	204s	148s	136s	224s
Add. peaks			258w											
			211w											
			165w					642sh				97w		
Data from	1	2	3	2	4	5	5	6	6	7, 10	8	9	9	12
Peak assigned by	11	11	11	11	11	12	12	11	11	7, 11	11	11	11	12

Notes: vs = very strong, s = strong, sh = shoulder, m = middle, w = weak, vw = very weak; 1 = Linton et al. 1999; 2 = Pinet et al. 1986; 3 = White 1974; 4 = Ko et al. 1989; 5 = Baran et al. 1986; 6 = Baran and Botto 1979; 7 = McMillan and Ross 1987; 8 = Ross and Navrosky 1988; 9 = Leinenweber et al. 1989; 10 = Chopelas 1999; 11 = Hofmeister 1993; 12 = this study.

ments (Beattie and Gilson 1970); the 226 and 497 cm^{-1} peaks are assigned to A_{1g} symmetry, and the 245, 292, 301, 411, and 612 cm^{-1} peaks are assigned to E_g symmetry (Table 5). Spectrum a in Figure 10 was taken from a synthetic sample of hematite powder (HMS3–R–1599 of Pfizer, Inc.). In addition to the 7 predicted Raman peaks, a broad band in the range of 1320–1270 cm^{-1} is observed in the Raman spectra of all forms of hematite, regardless of excitation laser wavelength (532 nm, 632.8 nm, 785 nm, etc.). The assignment of this peak has been controversial. It was assigned to two-magnon scattering by Hart et al. (1976) and Martin et al. (1977), and to two-phonon scattering of an IR-active mode at ~660 cm^{-1} by Shim and Duffy (2001). Clarifying this assignment is beyond the scope of this study, but this peak and the two sharp peaks at ~226 and ~293 cm^{-1} are easily observed hematite Raman features, even under poor sampling conditions; they are thus the most useful for identification of hematite. The exact positions of these peaks vary from sample to sample according to chemical composition. Figure 10b is a spectrum of hematite with 11.25 wt% TiO_2; all of its Raman peaks appear at lower Raman shifts and have increased peak widths.

Ilmenite has an hexagonal, close-packed oxygen framework similar to that of hematite, but the Fe and Ti cations are ordered among the 2/3 filled octahedral sites. This ordered distribution reduces the structural symmetry to $R\overline{3}$-C_{3i}^2, and 10 Raman active vibrational modes ($5A_g + 5E_g$) are predicted for the ilmenite structure (Table 3 of Ross and McMillan 1984). Numerous detailed Raman spectroscopic studies have been made on minerals with the ilmenite structure (e.g., $MgSiO_3$, $MgGeO_3$, $MgTiO_3$, $MnTiO_3$, $LiNbO_3$, $NaNbO_3$, $ZnTiO_3$, $CdTiO_3$, $ZnSiO_3$, and $ZnGeO_3$), a consequence of the importance of this structure to mantle mineralogy (Table 6, Linton et al. 1999; Pinet et al. 1986; White 1974; Ko et al. 1989; Baran et al. 1986; Baran and Botto 1979; McMillan and Ross 1987; Ross and Navrosky 1988; Leinenweber et al. 1989; Chopelas 1999; Hofmeister 1993). We found no report of the Raman spectrum of ilmenite itself ($FeTiO_3$), however. Spectra c and d in Figure 10 show typical spectral patterns and peak positions observed from two well-characterized $FeTiO_3$ ilmenite grains of different compositions (no. 497-g1 is an end-member ilmenite, no. 20 contains 9.75 wt% MgO, Table 1). Based on the published Raman spectra of other minerals with the ilmenite structure and the assignments made of their peaks (Table 6), we attribute the strongest Raman peak of $FeTiO_3$ ilmenite, ~683 cm^{-1}, to A_g symmetry as the symmetric stretching vibration of $Ti^{4+}O_6$ octahedra. The single strong and sharp peak at 224 cm^{-1} is characteristic of $FeTiO_3$ ilmenite. That peak also has A_g symmetry and likely is produced by the translational motion of the Fe cation in the crystal lattice. Three weaker Raman peaks are also observed at ~368, ~333, and ~270 cm^{-1} for these ilmenite grains (Table 6).

We can use the correlations between the Raman data in Table 6 and available data on the volumes of the unit cells, the bulk moduli, the lengths of the X-O bond (X being the cation that forms the most covalent bond with oxygen, e.g., Si, Ti, Ge) and the M-O bonds (M being the cation that forms the least covalent bond with oxygen, e.g., Mg, Fe, Mn, Cd, Zn), and the masses of the X and M cations to support the peak assignments for ilmenite. For example, the peak position shift of the A_g mode vibration from the ~683 cm^{-1} peak of $FeTiO_3$ to the ~800 cm^{-1} peak of $MgSiO_3$ correlates with the X-O bond length (R^2~0.80), cell volume (R^2 ~ 0.79), and bulk modulus (R^2~0.90), but not with the properties of M-O (R^2 ~0.1–0.2). This observation is consistent with the assignment for that peak, i.e., the stretching vibration of the XO_6 unit. In contrast, the peak position of the other A_g mode, which ranges from ~150 cm^{-1} in $CdTiO_3$ to ~350 cm^{-1} in $MgSiO_3$, correlates with the length of the M-O bond (R^2 ~ 0.91) and the mass of the M cation (R^2 ~ 0.80), but does not correlate with the properties of the X-O bonds, bulk moduli, and cell volumes (R^2 ~ 0.0–0.4). This observation is consistent with the assignment for that peak as the translational motion of the M cation within the crystal framework.

When other cations substitute for some of the Fe^{2+} in ilmenite, the mass differences induce a shift in the Raman peak positions. Using the major Raman peak positions from ilmenite no. 497-g1 and no. 20 (Figs. 10c and 10d) with published Raman data for geikielite $MgTiO_3$ (Linton 1999), a linear correlation (Fig. 11) can be found between the major A_g Raman peak positions and Mg/(Ti + Fe) ratios over the entire range of ilmenite-geikielite solid solution.

The ilmenite grains found in TS442 (lithology A) have compositions ($Ilm_{90\text{-}86}Geik_{6\text{–}10}Hem_{3\text{-}4}$) very near the end-member

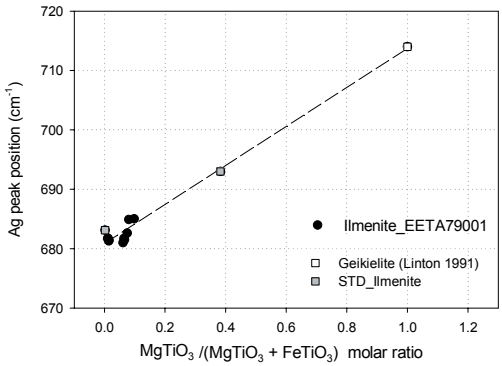

FIGURE 11. Correlation between the Raman A_g peak position of ilmenite-geikielite solid solutions and molar ratio of Mg/(Mg + Ti) on the basis of data from this study and the data of Linton et al. (1999).

composition of ilmenite. The compositions of ilmenite grains ($Ilm_{96}Geik_1Hem_2$) in EETA79001 TS357 (lithology B) are even closer to the end-member (Table 2). Together with the standard ilmenite samples, they form a very limited range in ilmenite-hematite solid solution, too close to examine the correlation between Raman peak positions and Ti/Fe ratios using this data set alone. The EETA79001 ilmenite grains have their major peaks in the range 684–687 cm^{-1}, intermediate to the major peaks of our standard ilmenite samples. The Raman and EMP data from EETA79001 ilmenite grains fall nicely on the correlation line between the Raman A_g peak position and the $MgTiO_3/(MgTiO_3 + FeTiO_3)$ ratio in Figure 11. The upward shift of the major Raman peak of ilmenite-geikielite solid solution (Ilm-Gk_{ss}) is caused by the mass effect of Mg^{2+} when it substitutes Fe^{2+} in ilmenite structure.

The Raman spectra in Figure 10 show that the difference in structure ($R\bar{3}c$ for hematite and $R\bar{3}$ for ilmenite) causes a significant change in the spectral pattern. Lindsley (1991), however, demonstrated that ilmenite and hematite can form complete solid solution $Fe^{3+}_{2-2x}Fe^{2+}_xTi^{4+}_xO_3$ at high temperature (above 960 °C). The consolute point lies below ~650 °C and is asymmetric toward hematite. We might therefore expect large differences in spectral pattern between titan-hematite and ferrian ilmenite, stemming from the contributions by both $Ti^{4+}O_6$ and $Fe^{3+}O_6$ octahedra (Table 3). It has been thought (Lindsley 1976) that at high temperature, end-member ilmenite and intermediate compositions of Ilm-Hem_{ss} would all have a disordered corundum structure $R\bar{3}c$ like hematite, because Fe^{3+} and Ti^{4+} would be distributed randomly in the octahedral sites, thus a hematite spectral pattern (Fig. 10 a) would be observed. However, when temperature decreases, the $R\bar{3}c$ hematite structure only can be quenched from solid solutions of low or intermediate Ti content (i.e., it would retain the spectral pattern of Fig. 10a), but cannot be quenched from end-member ilmenite or high-Ti ($x \geq 0.6$) solid solutions (Ishikawa 1958). For the latter, the high-temperature hematite structure would convert to the $R\bar{3}$ ilmenite structure (spectral pattern as in Fig. 10c) at low temperature (1100 °C for $x = 0.65$, 600 °C for $x = 0.45$). Therefore, we consider whether the Raman spectral pattern difference (Figs. 10a and 10c) can be used to classify Ilm-Hem_{ss} of different Fe/Ti ratios.

The end-member ilmenite and ferrian ilmenite grains ($x > 0.9$) in the EETA79001 thin sections, at ambient temperature, all yield the $R\bar{3}$ Raman spectral pattern of the ilmenite structure, which is consistent with expectations, as discussed above. In addition, Figures 10a and 10b show end-member hematite and titan-hematite ($x \sim 0.23$) both having the characteristic spectral pattern of $R\bar{3}c$ hematite, also consistent with expectation. However, in the ulvöspinel oxidation experiments discussed in the previous section, although a high-Ti Ilm-Hem_{ss} (with $x > 0.6$) is predicted to be one of the products, we never observed the spectral pattern of the ilmenite structure ($R\bar{3}$), even from sample spots that are visibly oxidized (Fig. 9; the Ilm-Hem_{ss} produced should have a composition very near end-member ilmenite, judging by the top dash line shown in Fig. 8). This observation does not seem consistent with the conclusions from the electrical conductivity measurements of Ishikawa (1958) that the hematite structure ($R\bar{3}c$) of high-Ti ($x \geq 0.6$) solid solutions could not be quenched. Perhaps such quenching occurred under our experimental conditions because the heated volumes were so small (~10^{-8} cm^3) that heat transfer and cooling were rapid once the laser beam was shut off. In any case, we cannot use the expected spectral pattern change near $x = 0.6$ to infer the chemistry of the solid solution ($Fe^{3+}_{2-2x}Fe^{2+}_xTi^{4+}_xO_3$) along the ilmenite-hematite join of Figure 8.

Figures 10a and 10b show that hematite peak positions shift downward with increasing Ti/Fe ratio. Downward peak position shifts also were observed in the spectra of Ilm-Hem_{ss} (with a spectral pattern of hematite) produced from the oxidation of end-member ulvöspinel (Fig. 9). Compared to the peak position of end-member hematite Fe_2O_3, the shifts can be as large as ~10 cm^{-1} for the 224 cm^{-1} peak and ~20 cm^{-1} for the 294 cm^{-1} peak. The decrease of the Ti/Fe ratio in Ilm-Hem_{ss} resulting from oxidation (dashed lines in Fig. 8) seems to be the cause for the downward shift in the peak position. The titan-hematite, however, has peak positions lower than those of end-member hematite, which is unexpected on the basis of the smaller mass of Ti relative to Fe, so Ti variation cannot be the only cause for the peak shifts. Local temperature increase and degradation of crystallinity also can cause the Raman peak to shift downward. Both effects are apparently present in this case and, for that reason, the peak positions of Ilm-Hem_{ss} cannot be used to evaluate the Ti/Fe ratio quantitatively in the manner that can be used for chromite.

Fe-Ti-Cr oxides observed in Raman point-count measurements from rock chips of EETA79001

Except for hematite, the Fe-Ti-Cr-oxides discussed here (chromite, magnetite, ulvöspinel, ilmenite, and their solid solutions) have similar spectral patterns: a major, wide peak in the range 600–800 cm^{-1}, and a few minor peaks at lower wavenumbers. To distinguish among these minerals, we rely on the positions of the major peak and the positions and patterns of the minor peaks. In a Raman point-counting procedure on unprepared rock surfaces, the minor peaks may be hard to detect because on a rough rock surface, most sampling points will not be in exact focus, and spectra with lower S/N would be obtained. We simulated this situation (fixed laser power, fixed integration time, and off-focus signal collection) on the EETA rock chips by placing only the first sampling point of the traverse in focus, thus simulating the conditions anticipated for planetary on-surface exploration.

Even without careful focus, we were able to use major peak positions to obtain substantial information about the Fe-Ti-Cr-oxides. The positions of the major Raman peaks (our data and those from Malézieux and Piriou 1988) of chromite, magnetite, ulvöspinel, ilmenite, and their solid solutions (synthetic and natural) are shown in Figure 12. A general trend of the major Raman peak positions related to their chemical composition is evident, and it helps us to further understand their Raman features. We can see that the type of cation in the octahedral sites (2nd row of horizontal bars on top of Fig. 12) of these Fe-Ti-Cr-oxides controls the positions of their major Raman peak in the 600–800 cm^{-1} region. For example, the three (Mg, Fe)Al_2O_4 samples with Al present in the octahedral site have major peaks at ~770 cm^{-1} (col. 1 in Fig. 12); Cr in the octahedral site shifts the major peaks of three (Mg, Fe)Cr_2O_4 samples to the 680–690 cm^{-1} range (col. 7 in Fig. 12); coexistence of Al and Cr in octahedral sites (synthetic and all natural chromites) produces a continuous spread of the major Raman peaks across the two extremes (col. 2–6 in Fig. 12). The positions of the major peaks also are affected by the Fe/(Fe + Mg) ratio in the tetrahedral sites (dashed lines between pairs of points of cols. 2 and 3 in Fig. 12), but the effects are second order (1st row of horizontal bars on top of Fig. 12). When Fe^{3+} resides in the octahedral site of magnetite, the major Raman peak shifts further downward into the 659–665 cm^{-1} range (col. 10 in Fig. 12); the substitution of Ti^{4+} for Fe^{3+} in ilmenite and ulvöspinel causes the major peak to shift upward above 680 cm^{-1} (col. 8 in Fig. 12). Mixed occupancy of the octahedral sites by Ti^{4+} and Fe^{3+} in Usp_Mgt_{ss} produces a spread of peak positions between ~650 and 690 cm^{-1} (col. 9 in Fig. 12). Using these trends of variation in the positions of the major Raman peaks along with peak widths and peak patterns (which are affected by overlapping with minor peaks), we can distinguish among the different Fe-Ti-Cr-oxides even using low S/N Raman spectra.

From Raman point-count measurements of rock sample no. 476 (1 chip, lithology A) and rock sample no. 482 (4 chips, lithology B) of EETA79001, we obtained some 1065 spectra from 11 point-count traverses. Of these spectra, 39 contain identifiable spectral peaks of Fe-Cr-Ti-oxides, including chromite, ilmenite, magnetite, and ulvöspinel. Typical spectra are shown in Figure 13. The mineral proportion of Fe-Ti-Cr-oxides inferred from the Raman point-count is ~3.2% in rock chip no. 476 and ~4.2% in rock chips no. 482, which are within the range found by McSween and Jarosewich (1988), i.e., 2.2–4.0% opaque (mostly

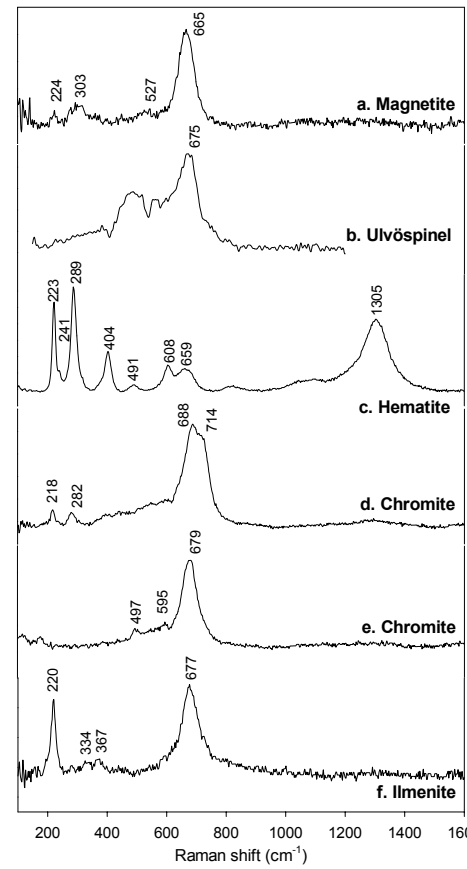

FIGURE 13. Raman spectra of Fe-Ti-Cr Oxides in EETA79001 rock chips from point-count measurements.

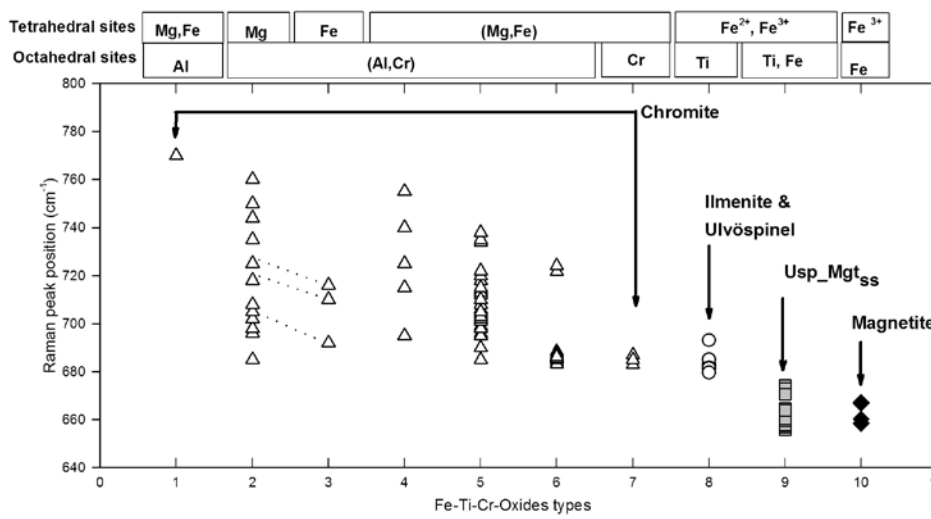

FIGURE 12. The distribution of major Raman peak positions of chromite, ilmenite, ulvöspinel, magnetite, and their solid solutions related to the types of octahedral and tetrahedral cations.

oxide) minerals in lithology A and 3.4–3.8% in lithology B. We found chromite, magnetite, and olivine in the rock chips that are mainly composed of lithology B (EETA79001, 482, four rock chips). These minerals have not been reported in this lithology previously; however, the lithologies are not everywhere clearly and sharply separated. We also found a trace of calcite from one of these rock chips. We were able to identify olivine and chromite by optical microscopy and electron microprobe analysis in a thin section (TS530) of that rock chip (one of the four chips of EETA79001, 482), which petrographically appears to be lithology A (contains xenocrysts and finer grain sizes).

In most cases, the spectral peaks of the Fe-Ti-Cr oxides appear in multiphase spectra accompanied by peaks from major and other accessory minerals, e.g., pyroxene, olivine, and merrillite. The multiphase spectra indicate that the Fe-Ti-Cr oxides in rock chips have mostly small grain sizes, except chromite. When chromite grains were detected in this set of Raman measurements, they appeared as single-phase spectra, meaning that chromite was the only phase in the sampled area excited by the laser beam. In addition, chromite spectra were obtained from three consecutive points in a linear traverse, whose points were spaced 100 μm apart. (The laser beam spot in these point-count measurements was ~6 μm diameter at focus. On the basis of our beam-profile measurement, the beam has a diameter of ~50 μm at ±200–250 μm away from the focal plane. The surface roughness of the rock chips is estimated ~ ±0.5 mm.) The observation of consecutive, single-phase spectra implies that the sizes of the chromite grains are on the order of 300 μm. This conclusion is consistent with the observations of optical microscopy and electron microprobe imaging, as shown in Figure 1c, which show a zoned xenocryst of chromite >350 μm in diameter.

In the Raman spectra of chromite from the rock chips (Figs. 13d and 13e), the major Raman peak positions occur in the range from 679 to 699 cm^{-1}, suggesting compositional variations. Using the correlation described in the previous section, the (Cr + Fe^{3+})/(Cr + Fe^{3+} + Al) ratios of these chromite grains range continuously between 0.75 and 1.0. This range is slightly wider than the compositional range measured by EMPA [(Cr + Fe^{3+})/(Cr + Fe^{3+} + Al) ~0.83 – 0.87] from the cores of the chromite grains in thin section TS442. The off-focus Raman measurements in the point-count procedure would sample a large area, thus the Raman signal from a zoned chromite (Fig. 4) may reflect a wider compositional range than that of a chromite core only.

Magnetite has not been reported in previous studies of EETA79001. The Raman spectrum of a magnetite (Fig. 13a), however, was obtained in a linear traverse across a rock chip of EETA79001, 482. The positions of major and minor peaks and spectral pattern indicate an end-member magnetite, when comparing them with Figure 5a of synthetic end-member magnetite and the general trend established by Figure 12. A titanomagetite $Mgt_{0.38}Usp_{0.44}$ grain was identified in TS442 of lithology A by EMP analysis (Table 2a), which is very different from other Mgt-Usp_{ss} grains in the same sample, but which is not an end-member magnetite.

Grains of a four-component (Chr-Spn-Usp-Mgt), solid-solution phase, which have smaller grain sizes, were partially oxidized at the fixed laser power (9 mW) used for the Raman point-count measurements. One of the oxidation products, hematite (or Ilm-Hem_{ss}), has a relatively high Raman cross section. The strong doublet (~224 and 294 cm^{-1}) of hematite-like phases occurs at substantially lower wavenumbers than the main Raman peaks of all major silicate phases, and we presume that this doublet is a proxy for Chr-Spn-Usp-Mgt_{ss} in our estimates of the mineral mode. Figure 14a shows one oxidized spot on synthetic magnetite. Figure 14b shows one spectrum taken from an oxidized spot in a high-Ti Usp-Mgt_{ss} grain in the thin section of EETA7900,357, which has all peaks shifted to lower wavenumbers. These spectra show that the Raman peak positions of Ilm-Hem_{ss} are related to its original chemistry. The oxidation product of the end-member magnetite (Fig. 14a) has the Raman peak positions of end-member hematite. The Raman peaks of the Ilm-Hem_{ss} produced by oxidation of the high-Ti Usp-Mgt_{ss} (Fig. 14b), however, are shifted to lower wavenumbers. The peaks of Ilm-Hem_{ss} produced by oxidation of end-member ulvöspinel (Figs. 9b and 9c) not only show a downshifted doublet, but a new peak occurring near 196 cm^{-1}. It appears that a rough estimate of the compositions of the original phases in a Mgt-Usp solid solution (magnetite, Fe-rich or Ti-rich Usp-Mgt_{ss}, or ulvöspinel) is possible on the basis of the peak-positions of the Ilm-Hem_{ss} produced by the oxidation, if all spectra were obtained in the same set of measurements. In EETA79001, however, 4-component (Chr-Spn-Usp-Mgt) solid solutions coexist with 2-component (Mgt-Usp) solid solutions, and both compositional mixing and structural mixing (inverse spinel and normal spinel) exist. Use of the peak position shifts to imply cation proportions is thus not straightforward in multi-component spinel systems such as EETA79001. In addition, some of these variations in peak position may be caused by temperature effects (Bersani et al. 1999).

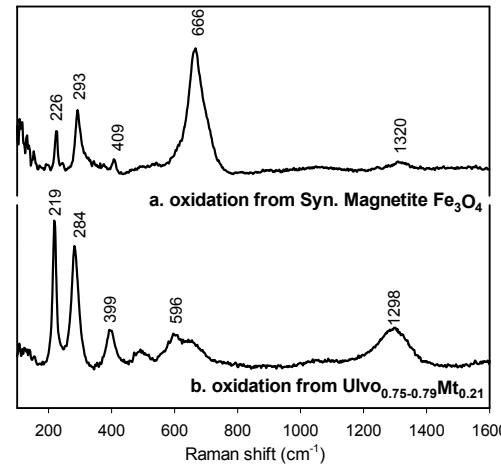

FIGURE 14. Raman peak positions of oxidation products from an end-member magnetite and an Usp-Mgt_{ss} grain.

The Raman peak positions (Fig. 13f) of ilmenite grains found in the rock chips of this meteorite are at or below 680 cm^{-1}, which suggests (Ti + Fe) ratios near 1.0, and Mg/(Mg + Fe) ratios near 0.0. These values are consistent with the EMP measurements on ilmenite grains that we found in both thin sections, EETA79001,442 and 79001,357 (Table 2).

Hematite has not been reported previously in EETA79001

(McSween and Jarosewich (1988)). One hematite spectrum (Fig. 13c) from one of the rock chips (no. 482, on which a calcite grain was identified, but not on the rock chip where magnetite was found) shows peak positions of end-member hematite and has spectral features very different from those of the oxidation products. All of the fundamental vibration peaks are present, the peaks are sharp, and the S/N level is high. This spectral pattern is characteristic of a well-crystallized hematite grain, which suggests that hematite may be a rare but original phase in this meteorite. The existence of hematite of this type would indicate oxidizing alteration on a local scale not produced by oxidation during analysis. We cannot, however, rule out the possibility of an origin for the hematite by slow weathering on Earth.

In summary, the Fe-Ti-Cr-oxides are relatively weak Raman scatterers, but they are detectable even under the relatively crude conditions of Raman point-count measurements on rock chips with irregular surfaces. Their detectability as observed in this work bodes well for observing these minerals during on-surface Raman measurements on Mars. Using knowledge developed through this study, we can distinguish among the different Fe-Ti-Cr-oxides and provide limited compositional information. This information, together with that derived from Raman studies of major silicates (e.g., Wang et al. 2000, 2003), aids in the identification of rock types and provides constraints on the crystallization history of rocks such as EETA79001. Because Fe-oxides and oxyhydroxides are likely products of aqueous alteration of primary igneous phases on Mars, their characterization can provide constraints on environments of alteration (deuteric, hydrothermal, and surface weathering), as well.

ACKNOWLEDGMENTS

The authors express special thanks to A.M. Hofmeister for providing synthetic magnetite and ulvöspinel samples and to J.D. Pasteris for constructive discussions. This work was supported in part by NASA grant NAG5–10703 and NAG5–12114. Critical reviews by M. Miyamoto and an anonymous reviewer led to significant improvements of this manuscript and are appreciated.

REFERENCES CITED

Armstrong, J.T. (1988) Quantitative analysis of silicate and oxide materials: comparison of Monte Carlo, ZAF, and φ (ρZ) procedures. Microbeam Analysis, 23, 239–46.

Akaogi, M., Ross, N.L., McMillan, P., and Navrotsky, A. (1984) The Mg_2SiO_4 polymorphs (olivine, modified spinel and spinel)—thermodynamic properties from oxide melt solution calorimetry, phase relations, and models of lattice vibrations. American Mineralogist, 69, 499–512.

Akimoto, S. (1954) Thermo-magnetic study of ferromagnetic minerals contained in igneous rock. Journal of Geomagnetism and Geoelectricity, 6, 1–14.

Baran, E.J. and Botto, I.L. (1979) Raman spectra of zinc titanate (IV) and cadmium titanate (IV). Zeitschrift fuer Anorganische und Allgemeine Chemie, 448, 188–192.

Baran, E.J., Botto, I.L., Muto, F., Kumada, N., and Kinomura, N. (1986) Vibrational spectra of the ilmenite modifications of lithium niobate and sodium niobate. Journal of Materials Science Letters, 5, 671–672.

Beattie, I.R. and Gilson, T.R. (1970) Single-crystal Raman spectra of nearly opaque materials. Iron (III) oxide and chromium (III) oxide. Journal of the Chemical Society [Section A: Inorganic, Physical, Theoretical] 6, 980–6.

Bersani, D., Lottici, P.P., and Montenero, A. (1999) Micro-Raman investigation of iron oxide films and powders produced by sol-gel syntheses. Journal of Raman Spectroscopy, 30, 355–360.

Brout, R. (1959) Sum rule for lattice vibrations in ionic crystals. Physical Review, 113, 43–44.

Busey, R.H. and Keller, O.L. Jr. (1964) Structure of the aqueous pertechnetate ion [determined] by Raman and infrared spectroscopy. Raman and infrared spectra of crystalline $KTcO_4$, $KReO_4$, Na_2MoO_4, Na_2WO_4, $Na_2MoO_4{\cdot}2H_2O$, and $Na_2WO_4{\cdot}2H_2O$. Journal of Chemical Physics, 41, 215–225.

Chevallier, R., Bolfa, J., and Mathieu, S. (1955) Titanomagnetites and ferromagnetic ilmenites. I. Optical, x-ray, crystallographic, and chemical study. Bulletin de la Société Française de Minéralogie et de Crystollographie, 78, 307–46.

Choi, C.H., Sharma, S.K., Lucey, P.G., and Muenow, D.W. (2003) Effect of particle size and laser-induced heating on the Raman spectra of Alpha Quartz grains. Accepted by Applied Spectroscopy.

Chopelas, A. (1999) Estimates of mantle-relevant Clapeyron slopes in the $MgSiO_3$ system from high-pressure spectroscopic data. American Mineralogist, 84, 233–244.

Chopelas, A. and Hofmeister, A.M. (1991) Vibrational spectroscopy of aluminate spinels at 1 atm. and of $MgAl_2O_4$ to over 200 kbar. Physics and Chemistry of Minerals, 18, 279–93.

Cynn, H., Sharma, S.K., Cooney, T.F., and Nicol, M. (1992) High-temperature Raman investigation of order-disorder behavior in the $MgAl_2O_4$ spinel. Physical Review B: Condensed Matter and Materials Physics, 45, 500–2.

De Faria, D.L.A., Silva, S.V., and De Oliveira, M.T. (1997) Raman microspectroscopy of some iron oxides and oxyhydroxides. Journal of Raman Spectroscopy, 28, 873–878.

Degiorgi, L., Blatter-Moerke, I., and Wachter, P. (1987) Magnetite: phonon modes and the Verwey transition. Physical Review B: Condensed Matter and Materials Physics, 35, 5421–4.

Edwards, H.G.M., Farwell, D.W., Grady, M.M., Wynn-Williams, D.D., and Wright, I.P. (1999) Comparative Raman microscopy of a Martian meteorite and Antarctic lithic analogues. Planetary and Space Science, 47, 353–362.

Emsley, J. (1993) The Element (second ed.). Oxford University Press Inc., New York.

Finger, L.W., Hazen, R.M., and Hofmeister, A.M. (1986) High-pressure crystal chemistry of spinel ($MgAl_2O_4$) and magnetite (Fe_3O_4): comparisons with silicate spinels. Physics and Chemistry of Minerals, 13, 215–220.

Gasparov, L.V., Tanner, D.B., Romero, D.B., Berger, H., Margaritondo, G., and Forro, L. (2000) Infrared and Raman studies of the Verwey transition in magnetite. Physical Review B: Condensed Matter and Materials Physics, 62, 7939–7944.

Grimes, N.W. and Collett, A.J. (1971) Correlation of infrared spectra with structural distortions in the spinel series Mg $(Cr_xAl_{2-x})O_4$. Physica Status Solidi B: Basic Research, 43, 591–599.

Hart, T.R., Temkin, H., and Adams, S.B. (1976) Light scattering in magnetite, Fe3O4. Proceedings of the 4th International Conference on Light Scattering Solids, 3rd, 254–8.

Haskin, L.A. and Wang, A. (2002) Study of rocks and Martian meteorite using the brassboard of the Mars Microbeam Raman Spectrometer (MMRS). Abstract No. 1742, Lunar and Planetary Science XXXIII, Lunar and Planetary Institute, Houston, Texas.

Haskin, L.A., Wang, A., Rockow, K.M., Jolliff, B.L., Korotev, R.L., and Viskupic, K.M. (1997) Raman spectroscopy for mineral identification and quantification for in-situ planetary surface analysis: a point count method. Journal of Geophysical Research, 102, 19,293–19,306.

Haskin, L.A., Wang, A., Jolliff, B.L., Wdowiak, T., Agresti, D., Lane, A.L., and Squyres, S. (2001) The Mars Microbeam Raman Spectrometer (MMRS). Abstract No. 1705, Lunar and Planetary Science XXXII, Lunar and Planetary Institute, Houston, Texas.

Hill, R.J., Craig, J.R., and Gibbs, G.V. (1979) Systematics of the spinel structure type. Physics and Chemistry of Minerals, 4, 317–339.

Hofmeister, A.M. (1991) Calculation on bulk moduli and their pressure derivatives from vibrational frequencies and mode Gruneisen parameters: solids with cubic symmetry or one-nearest-neighbor distance. Journal of Geophysical Research, 96, 16181–16203.

———(1993) IR reflectance spectra of natural ilmenite: comparison with isostructural compounds and calculation of thermodynamic properties. European Journal of Mineralogy, 5, 281–95.

Hofmeister, A.M. and Ito, E. (1992) Thermodynamic properties of $MgSiO_3$ ilmenite from vibrational spectra. Physics and Chemistry of Minerals, 18, 423–32.

Ishii, M., Hiraish, J., and Yamanaka, T. (1982) Structure and lattice vibrations of Mg-Al spinel solid solution, Physics and Chemistry of Minerals, 8, 64–68.

Ishikawa, Y. (1958) An order-disorder transformation phenomenon in the Fe-TiO_3-Fe_2O_3 solid solution series. Journal of Physical Society of Japan, 13, 828–837.

Kuebler, K.E., Wang, A., Abbott, K., and Haskin, L.A. (2001) Can we detect carbonate and sulfate minerals on the surface of Mars by Raman spectroscopy? Abstract No. 1889. Lunar and Planetary Science XXXII, Lunar and Planetary Institute, Houston, Texas.

Kuebler, K.E., Jolliff, B.L., Wang, A., and Haskin, L.A. (2002) A Raman spectroscopic study of samples from the May 2001 FIDO test site, Abstract no. 1536. Lunar and Planetary Science XXXIII, Lunar and Planetary Institute, Houston, Texas.

Kustova, G.N., Burgina, E.B., Sadykov, V.A., and Poryvaev, S.G. (1992) Vibrational spectroscopic investigation of the goethite thermal decomposition products. Physics and Chemistry of Minerals, 18, 379–82.

Ko, J., Brown, N.E., Navrosky, A., Prewitt, C.T., and Gasparik, T. (1989) Phase equilibrium and calorimetric study of the transition of MnTiO3 from the ilmenite to lithium niobate structure and implications for the stability field of

perovskite. Physics and Chemistry of Minerals, 16, 727–733.
Leinenweber, K., Navrotsky, A., McMillan, P., and Ito, E. (1989) Transition enthalpies and entropies of high pressure zinc metasilicates and zinc metagermanates. Physics and Chemistry of Minerals, 16, 799–808.
Lindsley, D.H. (1976) The crystal chemistry and structure of oxide minerals, as exemplified by the iron-titanium oxides. In Douglas Rumble III, Ed., Oxide Minerals, 3, p. L1–L60. Reviews in Mineralogy, Mineralogical Society of America, Washington, D.C.
———(1991) Experimental studies of oxide minerals. In D.H. Lindsley, Ed., Oxide Minerals, 25, p. 69–106. Reviews in Mineralogy, Mineralogical Society of America, Washington, D.C.
Linton, J.A., Fei, Y., and Navrotsky, A. (1999) The $MgTiO_3$-$FeTiO_3$ join at high pressure and temperature. American Mineralogist, 84, 1595–1603.
Liu, L.G., Mernagh, T.P., and Irifune, T. (1994) Raman spectra of high-pressure polymorphs of $MgSiO_3$ at various temperatures. Journal of Physics of the Earth, 42, 411–424.
Malézieux, J.M., and Piriou, B. (1988) Relation entre la composition chimique et le comportement vibrationnel de spinelles de synthèse et de chromites naturalles en microspectrométrie Raman, Bulletin Minéralogue, 111, 649–669.
Malézieux, J.M., Barbillat, J., Cervelle, B., Coutures, J.P., Couzi, M., and Piriou, B. (1983) Study of synthetic spinels of the Mg $(Cr_xAl_{2-x})O_4$ series and of natural chromites by Raman-laser microprobe. TMPM, Tschermaks Mineralogische und Petrographische Mitteilungen, 32, 171–85.
Martin, T.P., Merlin, R., Huffman, D.R., and Cardona, M. (1977) Resonant two magnon Raman scattering in a-iron (III) oxide. Solid State Communications, 22, 565–7.
McMillan, P. and Akaogi, M. (1987) Raman spectra of β-Mg_2SiO_4 (modified spinel) and γ-Mg_2SiO_4 (spinel). American Mineralogist, 72, 361–364.
McMillan, P.F. and Ross, N.L. (1987) Heat capacity calculations for Al_2O_3 corundum and $MgSiO_3$ ilmenite. Physics and Chemistry of Minerals, 14, 225–234.
McSween, H.Y. Jr. and Jarosewich, E. (1983) Petrogenesis of the Elephant Moraine A79001 meteorite: multiple magma pulses on the shergottite parent body. Geochimica et Cosmochimica Acta, 47, 1501–1513.
Mittlefehldt, D.W., Lindstrom, D.J., Lindstrom, M.M., and Martinez, R.R. (1999) An impact-melt origin for lithology A of Martian meteorite Elephant Moraine A79001. Meteoritics and Planetary Science, 34, 357–367.
Neel, L. (1955) Some Theoretical aspects of rock magnetism, Advanced Physics, 4, 191–243.
O'Reilly, W. and Banerjee, S.K. (1965) Cation distribution in titanomagnetites (1-x)Fe_3O_4-xFe_2TiO_4. Physics Letters, 17, 237–238.
Pinet, M., Smith D.C., and Boyer, H. (1986) Raman fingerprinting of opaque and semi-opaque minerals: the natural system Geikielite-ilmenite-pyrophanite (GIP), TERRA Cognita, 7, 18.
Reynard, B., and Guyot, F. (1994) High-temperature properties of geikielite ($MgTiO_3$-ilmenite) from high-temperature high-pressure Raman spectroscopy—some implications for $MgSiO_3$-ilmenite. Physics and Chemistry of Minerals, 21, 441–450.
Reynard, B., and Rubie, D.C. (1996) High-pressure, high-temperature Raman spectroscopic study of ilmenite-type $MgSiO_3$. American Mineralogist, 81, 1092–1096.
Robinson, K., Gibbs, G.V., and Ribbe, P.H. (1971) Quadratic elongation: a quantitative measure of distortion in [mineral] coordination polyhedra. Science,172, 567–570.
Ross, N.L. and McMillan, P. (1984) The Raman spectrum of magnesium silicate ($MgSiO_3$) ilmenite. American Mineralogist, 69, 719–721.
Ross, N.L. and Navrotsky, A. (1987) The Mg_2GeO_4 [magnesium germanate] olivine-spinel phase transition. Physics and Chemistry of Minerals, 14, 473–481.
———(1988) Study of the $MgGeO_3$ polymorphs (orthopyroxene, clinopyroxene, and ilmenite structures) by calorimetry, spectroscopy, and phase equilibria. American Mineralogist, 73, 1355–1365.
Shim, S.H. and Duffy, T.S. (2002) Raman spectroscopy of Fe_2O_3 to 62 GPa. American Mineralogist, 87, 318–326.
Smyth, J.R. and Bish, D.L. (1988) Crystal structures and cation sites of the rock-forming minerals, Allen & Unwin, Inc., Boston.
Wang, A. and Valentine, R.B. (2002) Seeking and Identifying Phyllosilicates on Mars—A simulation study. Abstract No. 1370, Lunar and Planetary Science XXXIII, Lunar and Planetary Institute, Houston, Texas.
Wang, A., Dhamelincourt, P., and Silvi, B. (1993) A high P-T structural form of chromite found as inclusion in diamond. Geological Society of America Abstracts with Programs, 25, 6, A–217.
Wang, A., Han, J., Guo, L., Yu, J., and Zeng, P. (1994) A database of standard Raman spectra of mineral and related inorganic crystals. Applied Spectroscopy, 48, 959–968.
Wang, A., Jolliff, B.L., and Haskin, L.A. (1995) Raman spectroscopy as a method for mineral identification on lunar robotic exploration missions. Journal of Geophysical Research, 100, 21189–21199.
Wang, A., Haskin, A.L., and Cortez, E. (1998) A Raman spectroscopic sensor for in situ mineral characterization on planetary surface, Applied Spectroscopy, 52, 477–487.
Wang, A., Jolliff, B.L., and Haskin, L.A. (1999a) Raman spectroscopic characterization of a Martian SNC meteorite: Zagami. Journal of Geophysical Research, 104, 8509–8519.
———(1999b) Raman spectroscopic characterization of a highly weathered basalt: igneous mineralogy, alteration products, and a microorganism. Journal of Geophysical Research, 104, 27,067–27,077.
Wang, A., Haskin, L.A., Kuebler, K.E., and Jolliff, B.L., and Walsh M. M. (2001a) Raman spectroscopic detection of graphitic carbon of biogenic parentage in an ancient South African chert. Abstract No. 1423, Lunar and Planetary Science XXXII, Lunar and Planetary Institute, Houston, Texas.
Wang, A., Kuebler, K.E., Freeman, J., and Jolliff, B.L. (2001b) Preliminary Raman spectroscopic survey on a Martian meteorite—Los Angeles, Abstract No. 1431, Lunar and Planetary Science XXXII, Lunar and Planetary Institute, Houston, Texas.
Wang, A., Kuebler, K.E., and Jolliff, B.L. (2001c) Raman spectroscopy of opaque minerals and applications to EETA79001 Martian meteorite. Abstract No. 1615, Lunar and Planetary Science XXXII, Lunar and Planetary Institute, Houston, Texas.
Wang, A., Freeman, J., and Kuebler, K.E. (2002) Raman Spectroscopic Characterization of Phyllosilicates. Abstract No.1374, Lunar and Planetary Science XXXIII, Lunar and Planetary Institute, Houston, Texas.
Wang, A., Haskin, L.A., Lane, A.L., Wdowiak, T.J., Squyres, S.W., Wilson, R.J., Hovland, L.E., Manatt, K.S., Raouf, N., and Smith, C.D. (2003) Development of the Mars Microbeam Raman Spectrometer (MMRS). Journal of Geophysical Research, 108, 5005, doi: 10.1029/2002JE001902.
Wang, A., Kuebler, K.E., Jolliff, B.L., and Haskin, L.A. (2004) Mineralogy of a Martian Meteorite as Determined by Raman Spectroscopy. Journal of Raman Spectroscopy, in press.
Wdowiak, T.J., Agresti, D.G., Mirov, S.B., Kudryavtsev, A.B., Beegle, L.W., DesMarais, D.J., and Trarpe, A.F. (1997) Identification of ancient carbonaceous cherts on Mars using Raman spectroscopy. In Clifford, S.M., Treiman, A.H., Newsom, H.E. and Farmer, J.D., Eds., Conference on Early Mars: Geologic and Hydrologic Evolution, Physical and Chemical Environments, and the implications for life, p. 81–82. Lunar and Planetary Institute Contribution No. 916, Houston, Texas.
Wechsler, B.A., and Prewitt, C.T. (1984) Crystal structure of ilmenite ($FeTiO_3$) at high temperature and at high pressure. American Mineralogist, 69, 176–185.
White, W.B. (1974) Order-disorder effects. In The Infrared Spectra of Minerals, ed. Farmer V. C., Mineralogical Society Monograph 4, Adlard & Son Ltd., at the Bartholomew Press, Dorking, Surrey.
White, W.B. and DeAngelis, B. A. (1967) Interpretation of the vibrational spectra of spinels. Spectrochemica Acta, 23A, 985–995.
Wynn-Williams, D.D. and Edwards, H.G.M. (2000) Proximal analysis of regolith habitats and protective biomolecules in situ by laser Raman spectroscopy: Overview of terrestrial Antarctic habitats and Mars analogs. Icarus, 144, 486–503.
Xu, J., Huang, E., Lin, J., and Xu, L.Y. (1995) Raman study at high pressure and the thermodynamic properties of corundum: Application of Kieffer's model. American Mineralogist, 80, 1157–1165.
Yamanitsu, T. and Ishii, M. (1986) Raman scattering and lattice vibrations of Ni_2SiO_4 spinel at elevated temperature, Physics and Chemistry of Minerals, 13, 156–160.

MANUSCRIPT RECEIVED APRIL 30, 2003
MANUSCRIPT ACCEPTED JANUARY 25, 2004
MANUSCRIPT HANDLED BY THOMAS DUFFY